Local lubrication model for spherical particles within incompressible Navier-Stokes flows

B. Lambert,* L. Weynans,† and M. Bergmann†
Memphis Team, INRIA, F-33400 Talence, France

(Received 13 July 2017; revised manuscript received 21 December 2017; published 28 March 2018)

The lubrication forces are short-range hydrodynamic interactions essential to describe suspension of the particles. Usually, they are underestimated in direct numerical simulations of particle-laden flows. In this paper, we propose a lubrication model for a coupled volume penalization method and discrete element method solver that estimates the unresolved hydrodynamic forces and torques in an incompressible Navier-Stokes flow. Corrections are made locally on the surface of the interacting particles without any assumption on the global particle shape. The numerical model has been validated against experimental data and performs as well as existing numerical models that are limited to spherical particles.

DOI: 10.1103/PhysRevE.97.033313

I. INTRODUCTION

Mixtures of solid particles in a liquid, i.e., suspensions, are a type of two-phase flow that appear in various industrial applications as well as in natural flows. For instance, sedimentation in rivers or near-coast influences the flow. By understanding the dynamics of the bed-load transport, the evolution of the river-stream can be forecast to prevent abnormal erosion or obstruction of waterways [1,2]. Macroscopic suspensions are also relevant in several industrial applications, such as nuclear waste processing, water treatment, and reinforced plastics manufacturing. For dense mixtures as uncured solid rocket fuel or concretes, a high concentration of solid particles is desired without compromising the rheological properties and the flowing behavior of the mixture.

Over the years, several numerical methods have been developed to simulate particle-laden flows at different scales. However, due to the importance of the fluid-particle interactions, only microscale methods are relevant since they fully resolve the flow around each particle. Since the computational cells are larger than the particle size, macroscale methods, such as Stokesian dynamics (SD) [3,4] or force-coupling method (FCM) [5,6], cannot capture the essential details of the flow. Both methods depend on a truncated multipole expansion of the Stokes equations. Thereby, they are usually suited only for specific particle shapes and are inherently restricted to viscous flows. From the limitations of macroscale methods, direct numerical simulation (DNS) has emerged as an appealing alternative, reachable thanks to modern improvements of the computer performances. By solving the governing equations (Navier-Stokes equations) directly without any further assumptions, DNS enables microscale simulations of arbitrary particle shape at the numerical method accuracy level. The DNS methods can be divided into two classes. The first class considers boundary-fitted approach [7,8], where the fluid fills the meshed domain. If the mesh elements are small enough, this approach enables an accurate computation of the boundary layers and interactions between particles. However, as the particles move, the domain needs to be constantly adapted leading to possibly complex and expansive remeshing issues. The computational cost of the remeshing limits three-dimensional simulations to about a hundred particles [8]. In contrast, the second class of DNS methods considers non-boundary-fitted meshes which are more suited to numerical simulations using a large number of particles. In this approach, the whole domain is discretized on an Eulerian fixed grid where the particles are embedded. Several techniques are available to simulate the particulate flow using fictitious domain methods [9–15], encompassing lattice Boltzmann methods [16], immersed boundary methods (IBM) [17,18] and volume penalization method (VP) [19]. In this paper, numerical simulations have been performed using a VP approach coupled with a discrete element method (DEM) [20]. The DEM is widely used for granular flow simulation. In this fully coupled method, the particles are tracked using Lagrangian markers. The particle dynamics are solved using Newton's laws.

Although microscale methods are able to capture flow details, they are challenged by some short-range effects. As two particles are moving toward each other they start to interact throughout the fluid as the separation distance $a\epsilon$ (where a denotes the particle radius) becomes small. This well-known lubrication effect is due to the draining of interstitial fluid in the gap between the two interacting particles. The normal and tangential components of the lubrication force diverge as the particles collide (ϵ tends to 0) as ϵ^{-1} and $\log(\epsilon)$, respectively. At low Reynolds number values, DNS methods are able to resolve these lubrication forces if the grid spacing is small enough. Typically, the grid spacing should be at least smaller than $10^{-3}a$ to capture lubrication effects [21]. The computational costs make long-term simulations of concentrated suspensions prohibitive. Most simulations are performed on meshes with a grid spacing of about $10^{-1}a$, meaning that the accuracy of the description of the lubrication effects drops as the particles come

*Also at University of Bordeaux, IMB, UMR 5251, F-33400 Talence, France; baptiste.lambert@inria.fr
†Also at University of Bordeaux, IMB, UMR 5251, F-33400 Talence, France; CNRS, IMB, UMR 5251, F-33400 Talence, France.

in near contact. Therefore, a numerical lubrication model is usually introduced to balance the unresolved lubrication forces. In the simplest lubrication model, the theoretical lubrication force known for two spherical particles (normal [22] and tangent [23] components) is added to the computed hydrodynamic force [24]. This approach considers that lubrication cannot be captured by the flow solver. However, by adding the theoretical lubrication force, the lubrication partially captured by the solver is counted twice. A more accurate approach is suggested in Stokesian dynamics, where hydrodynamic forces are split into a long- and a short-range actions. The short-range actions are also known as lubrication. Hence long-range actions are provided by the solver and short-range actions are modeled via the lubrication theory, avoiding an overestimation of the total hydrodynamic forces. However, this decomposition is not easy to adapt to DNS since the long-range hydrodynamics is not explicitly known. A common technique [21,25] is to perform off-line simulations of two isolated particles using a refined mesh without any lubrication model, for different configurations and the normalized separation distance ϵ, to estimate the unresolved part of the lubrication forces. From these off-line simulations and the lubrication theory, a tabulation of lubrication corrections is created. Hence, the lubrication model for on-line simulations estimates the correction to perform from the tabulation. The accuracy of this method depends on the quality of the tabulation and the diversity of the off-line samples used to create it. Thus, these methods are usually used for monodisperse suspensions of spherical particles since only the tabulation of a single parameter is required. Theoretically, the tabulation of more general suspension models is also possible [26]. However, the computational cost involved to generate an accurate multi-parameter tabulation makes general suspensions unachievable in reasonable CPU time.

In this paper, a lubrication model for incompressible Navier-Stokes flows without tabulation is proposed. The key-point of our model is a local correction of the lubrication effects on the particle surface without any assumption on the global particle geometry. This article is organized as follows. In Sec. II, we present the theoretical background of our model based on a similar framework than the lubrication theory. Section III briefly introduces the soft-sphere model developed by Walton *et al.* [27] for particle collisions. Section IV details the numerical method used to solve the particle laden flow. Finally, our local lubrication correction model is compared to other lubrication models and validated using two experimental cases in Sec. V.

II. THEORETICAL FRAMEWORK FOR LUBRICATION MODEL

The local lubrication correction model developed in this paper is based on a theoretical framework used in the classical lubrication theory [22,23]. Furthermore, the analytic expressions of the local lubrication forces and torques have been obtained using the same method as used in the lubrication theory. Therefore, the reader will be referred to the original references for mathematical calculations which are identical to the lubrication theory.

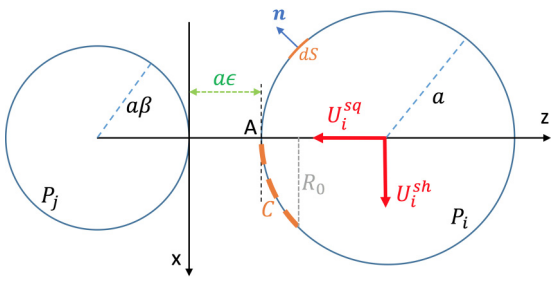

FIG. 1. Sketch of two particles in interaction.

A. Squeezing motion of rigid spheres

Two smooth particles of radii a and βa (with $\beta > 0$) immersed in an infinite fluid domain are considered. One of the particles (P_i) is moving at the constant velocity $\mathbf{U}_i = -U_i^{\mathrm{sq}}\mathbf{e_z}$ toward the second stationary particle (P_j) (Fig. 1). The surfaces of P_i and P_j are denoted Γ_i and Γ_j. The gap between the two particles is denoted $a\epsilon$ with $0 < \epsilon \ll 1$.

We consider the flow in the gap in the neighborhood of the contact point A, such that the Reynolds number in the gap is small ($\mathrm{Re} = \rho U_i^{\mathrm{sq}} a\epsilon/\mu \ll 1$). Hence, the flow can be modeled by the Stokes Eq. (1):

$$\begin{aligned} &\mu\Delta\mathbf{u} = \boldsymbol{\nabla} p, \\ &\boldsymbol{\nabla}\cdot\mathbf{u} = 0, \\ &\mathbf{u}\restriction_{\Gamma_i} = \mathbf{U}\restriction_{\Gamma_i}, \\ &\mathbf{u}\restriction_{\Gamma_j} = \mathbf{U}\restriction_{\Gamma_j}, \\ &\lim_{r\to+\infty} p = 0, \end{aligned} \tag{1}$$

where $\mathbf{u}$ is the velocity field, p is the pressure field, ρ is the fluid density, μ the fluid dynamic viscosity, and the particle surface velocities are $\mathbf{U}\restriction_{\Gamma_i} = -U_i^{\mathrm{sq}}\mathbf{e_z}$ and $\mathbf{U}\restriction_{\Gamma_j} = 0$.

The system Eq. (1) is transformed by introducing the Stokes stream-function ψ in the cylindrical coordinate system (r,θ,z) defined such that [28–30] $(u_r,u_\theta,u_z) = (\frac{1}{r}\partial_z\psi, 0, -\frac{1}{r}\partial_r\psi)$:

$$\Leftrightarrow \begin{cases} \Phi^4(\psi) = 0, \\ \psi\restriction_{\Gamma_i} = \frac{1}{2}U_i^{\mathrm{sq}} r^2, \\ \psi\restriction_{\Gamma_j} = 0, \end{cases} \tag{2}$$

with $\Phi^2(\cdot) = r\partial_r[\frac{1}{r}\partial_r(\cdot)] + \partial_z^2(\cdot)$. The stream-function ψ solution of Eq. (2) can be found near the particle surface Γ_i via the Taylor expansion of ψ as detailed by Jeffrey *et al.* [29].

The lubrication force is due to the hydrodynamic effect of the interaction of the given particle with a nearby obstacle. Thereby, the force is given by the action of the fluid stress on a particle surface when this particle and the interacting obstacle are isolated in an unbounded domain (flow field at rest far from the particles). The lubrication force is directly obtained by integrating the fluid stress σ acting on the particle surface,

$$\sigma = -pI + \mu[\boldsymbol{\nabla}\mathbf{u} + (\boldsymbol{\nabla}\mathbf{u})'], \tag{3}$$

with I the identity matrix.

Due to the symmetry of the flow, only the stress induced by a force acting parallel to the axis of revolution (Oz) is relevant.

Thus, the lubrication force on P_i is

$$\mathbf{F}_i^{\text{lub}} = \left[\int_{\Gamma_i} (\sigma \cdot \mathbf{n}) \cdot \mathbf{e_z}\, dS\right]\mathbf{e_z}, \tag{4}$$

with $\mathbf{n}$ the outgoing unit vector of the surface element dS of the particle P_i as shown in Fig. 1.

In any plane containing the axe (Oz), the particle surfaces Γ_i and Γ_j can be characterized, near the contact point, as follows:

$$\begin{aligned} z_i(r) &= a(1+\epsilon) - \sqrt{a^2 - r^2} \sim a\epsilon + \frac{r^2}{2a} + O(r^4), \\ z_j(r) &= -\beta a + \sqrt{\beta^2 a^2 - r^2} \sim -\frac{r^2}{2\beta a} + O(r^4). \end{aligned} \tag{5}$$

To simplify these expressions, the stretched coordinates are introduced:

$$\begin{aligned} R &= \frac{r}{a\sqrt{\epsilon}}, \\ Z &= \frac{z}{a\epsilon}, \\ H &= Z_i - Z_j = 1 + \frac{1+\beta}{2\beta} R^2 + O(\epsilon), \end{aligned} \tag{6}$$

where Z_i and Z_j are $z_i(r)$ and $z_j(r)$ from Eq. (5) in the stretched coordinates, respectively.

Via straightforward calculations and simplifications detailed by Happel *et al.* [31], the lubrication force on the particle P_i is expressed as a function of ψ, solution of Eq. (2), as follows:

$$\mathbf{F}_i^{\text{lub}} = \pi\mu \int_C r^3 \partial_n \left(\frac{\Phi^2(\psi)}{r^2}\right) ds\, \mathbf{e_z}, \tag{7}$$

where $ds = \sqrt{\epsilon}(1 + \frac{1}{2}\epsilon R^2) dR + O(\epsilon^{3/2})$ and $\partial_n = -\epsilon^{-1}\partial_Z + \frac{1}{2}R^2\partial_Z + R\partial_R + O(\epsilon)$ in the stretched coordinates [28,29,31] Eq. (6). The inner region is defined by the neighborhood $C = [0, R_0]$ of the contact point A (see Fig. 1). In this region, the Stokes stream-function ψ is solution of Eq. (2). Therefore, the dominant order (in ϵ) of the lubrication force in the inner region is given by

$$\frac{\mathbf{F}_i^{\text{lub,in}}}{\pi\mu a U_i^{\text{sq}}} = -\frac{6R_0^4}{4H_0^2}\frac{1}{\epsilon}\mathbf{e_z} + O(1). \tag{8}$$

To obtain the lubrication force on the whole surface, the lubrication force on the outer region needs to be added to the contribution from the inner region Eq. (8). This can be done by solving Eq. (7) with ψ solution of a Stokes problem in the outer region and matching this solution to the solution in the inner region [29]. Another approach is to match the inner solution Eq. (8) with a solution on the outer region obtained via a detailed numerical simulation [28]. At the end, both methods give the dominant order of the total lubrication force as follows:

$$\frac{\mathbf{F}_i^{\text{lub}}}{\pi\mu a U_i^{\text{sq}}} = -\frac{6}{\epsilon}\mathbf{e_z} + O(1). \tag{9}$$

B. Shearing motion of rigid spheres

As for the squeezing motion, two smooth particles of radii a and βa, with $\beta > 0$, are immersed in an infinite domain of fluid. The particle P_i is now moving near the stationary particle P_j at the velocity $\mathbf{U}_i = U_i^{\text{sh}}\mathbf{e_x}$ (see Fig. 1). The surfaces of P_i and P_j are denoted Γ_i and Γ_j. The gap between the two particles is denoted by $a\epsilon$ $(0 < \epsilon \ll 1)$ such that the gap Reynolds number is small $(\text{Re} = \rho U_i^{\text{sh}} a\epsilon/\mu \ll 1)$.

According to Kim *et al.* [28], symmetries in the flow field in the gap suggest that $(\mathbf{u}, p)$ can be written in the cylindrical coordinate system $(\mathbf{e_r}, \mathbf{e}_\theta, \mathbf{e_z})$ as follows:

$$\begin{aligned} u_r &= U_i^{\text{sh}} U(r,z)\cos(\theta), \\ u_\theta &= U_i^{\text{sh}} V(r,z)\sin(\theta), \\ u_z &= U_i^{\text{sh}} W(r,z)\cos(\theta), \\ p &= \frac{\mu U_i^{\text{sh}}}{a} P(r,z)\cos(\theta), \end{aligned} \tag{10}$$

where the angle θ is defined such that $\mathbf{e_r} = \cos(\theta)\mathbf{e_x} + \sin(\theta)\mathbf{e_y}$, and U, V, W, and P are unknown functions such that the velocity and pressure fields are solutions of the Stokes problem Eq. (1). Via regular expansion of U, V, W, and P and the Taylor expansion of $\mathbf{u}$ and p at the particle surface Γ_i, the dominant order (in ϵ) of $(\mathbf{u}, p)$ solution of Eq. (1) can be found as detailed by O'Neill *et al.* [23]. In particular, the dominant orders of U, V, and P are

$$\begin{aligned} U_0(R,Z) &= -\frac{1}{2}\frac{dP_0}{dR}(Z - Z_j)(Z_i - Z) + \frac{Z - Z_j}{H}, \\ P_0(R) &= \frac{6R}{5H^2}\left(1 - \frac{1}{\beta}\right), \\ V_0(R,Z) &= -\frac{1}{2}\frac{P_0}{R}(Z - Z_j)(Z_i - Z) - \frac{Z - Z_j}{H}, \end{aligned} \tag{11}$$

if $(\mathbf{u}, p)$ is solution of Eq. (1) with the boundary conditions $\mathbf{U}\restriction_{\Gamma_i} = U_i^{\text{sh}}\mathbf{e_x}$ and $\mathbf{U}\restriction_{\Gamma_j} = 0$.

As for the squeezing motion, the lubrication force and torque are directly obtained by integration of the fluid stress σ [see Eq. (3)] over the particle surface Γ_i. Due to the symmetry of the flow, only the component of the force according to the (Ox) is nonzero. Hence, the lubrication shear force and torque acting on an element of surface dS of Γ_i are given by

$$\begin{aligned} \mathbf{F}_i^{\text{lub}} &= \left(\int_{\Gamma_i} (\sigma \cdot \mathbf{n}) \cdot \mathbf{e_x}\, dS\right)\mathbf{e_x}, \\ \mathbf{T}_i^{\text{lub}} &= \int_{\Gamma_i} (\sigma \cdot \mathbf{n}) \wedge \mathbf{e_y}\, dS. \end{aligned} \tag{12}$$

By substitution of $(\mathbf{u}, p)$, expressed as in Eq. (10), solution of the Stokes Eq. (1), the dominant orders (in ϵ) of the lubrication force and torque in the inner region are found:

$$\frac{\mathbf{F}_i^{\text{lub,in}}}{a\mu\pi U_i^{\text{sh}}} = \int_0^{R_0} [-P_0 R + \partial_Z V_0 - \partial_Z U_0] R dR\, \mathbf{e_x} + O(\epsilon), \tag{13}$$

$$\frac{\mathbf{T}_i^{\text{lub,in}}}{a^2\mu\pi U_i^{\text{sh}}} = \int_0^{R_0} [\partial_Z U_0 - \partial_Z V_0] R dR\, \mathbf{e_y} + O(\epsilon). \tag{14}$$

III. COLLISION MODEL

In a Stokes flow, the contact between obstacles is theoretically impossible due to the lubrication singularity. However,

a collision model needs to be considered for physical and numerical purposes.

From a physical perspective, the lubrication effect alone cannot explain some phenomena such as the rebound of particle onto a wall, which occurs at the Stokes number above roughly [24] $\mathrm{St}_d = \frac{\rho_\mathrm{p} d U_\mathrm{c}}{9\mu} \approx 10$, with ρ_p, d, and U_c the particle density, diameter, and impact velocity, respectively. The collision model is seen here as a "low cost" model to mimic the effect of the particle deformation on its trajectory. Furthermore, real surfaces are never perfectly smooth, meaning that contact can occur at the particle roughness scale or at the lubrication film breakdown scale (when the separation distance is close to the fluid particle characteristic size).

From a numerical point of view, a cutoff distance for the lubrication forces is usually introduced to ensure the model stability. This cutoff distance prevents the lubrication force Eq. (9) to diverge as the particle collides with an obstacle. A control on the time step to avoid contact due to time discretization errors is not an option. Indeed, an adaptive time step would certainly improve the capture of the lubricating effects, but in case of colliding particles at the Stokes number regime $\mathrm{St}_d > 10$, the time step would keep decreasing asymptotically to zero. Therefore, a lubrication cutoff distance and a collision model need to be introduced for stable and finite time simulations.

The collision model chosen here is based on the soft-sphere approach used by Costa *et al.* [32]. The deformation of particles during contact is modeled by the overlap between a particle and an obstacle (particle or wall). From the overlap measurement, normal and tangential contact forces are computed using a mass-spring-dashpot system and a Coulomb-type threshold for the tangential component. For a given particle P_i, collision forces $\mathbf{F}_i^{\mathrm{coll}}$ and torque $\mathbf{T}_i^{\mathrm{coll}}$ are decomposed as

$$\begin{aligned} \mathbf{F}_i^{\mathrm{coll}} &= \sum_{j\neq i} \mathbf{F}_{i,j} + \mathbf{F}_{i,\mathrm{wall}}, \\ \mathbf{T}_i^{\mathrm{coll}} &= \sum_{j\neq i} \mathbf{T}_{i,j} + \mathbf{T}_{i,\mathrm{wall}}, \end{aligned} \tag{15}$$

where $\mathbf{F}_{i,j}$ is the collision force of the interacting particles P_i and P_j, $\mathbf{F}_{i,\mathrm{wall}}$ is the collision force of P_i with a wall. $\mathbf{T}_{i,j}$ and $\mathbf{T}_{i,\mathrm{wall}}$ are the corresponding collision torques. The force and the torque on P_i resulting from the particle-particle interactions between P_i and P_j are defined (as follows) using a local system of coordinates $(\mathbf{e_n}, \mathbf{e_t})$ (Fig. 2):

$$\begin{aligned} \mathbf{F}_{i,j} &= \mathbf{F}_n + \mathbf{F}_t, \\ \mathbf{T}_{i,j} &= a\mathbf{e_n} \wedge (\mathbf{F}_t), \end{aligned} \tag{16}$$

with

$$\begin{aligned} \mathbf{F}_n &= -\boldsymbol{\delta_n} k_\mathrm{n} - \gamma_\mathrm{n}(\mathbf{U}_{i,j}\cdot\mathbf{e_n})\mathbf{e_n}, \\ \mathbf{F}_t &= \min(\| -\boldsymbol{\delta_t} k_\mathrm{t} - \gamma_\mathrm{t}(\mathbf{U}_{i,j}\cdot\mathbf{e_t})\mathbf{e_t}\|, \|\mu_c \mathbf{F}_n\|)\mathbf{e_t}, \end{aligned} \tag{17}$$

where a is the radius of P_i, $\boldsymbol{\delta_n}$ (respectively, $\boldsymbol{\delta_t}$) is the normal (respectively, tangential) overlap, k_n (respectively, k_t) is the normal (respectively, tangential) stiffness, μ_c is the friction coefficient, and γ_n (respectively, γ_t) is the normal (respectively, tangential) damping coefficient of the spring-dashpot model. The relative velocity of the two particles $\mathbf{U}_{i,j}$ at the contact point is given by $\mathbf{U}_{i,j} = \mathbf{U}_i + a\omega_i \wedge \mathbf{e_n} - (\mathbf{U}_j - a\beta\omega_j \wedge \mathbf{e_n})$.

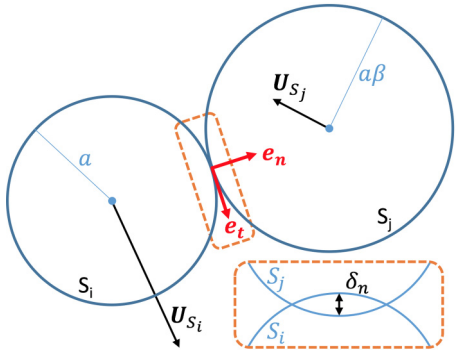

FIG. 2. Contact of two particles with notations associated to the soft sphere model.

The normal overlap distance $\boldsymbol{\delta_n}$ is given by

$$\boldsymbol{\delta_n} = \max(0, a(1+\beta) + \epsilon_{\mathrm{col}}(a+\beta a) - \|\mathbf{X}_i - \mathbf{X}_j\|)\mathbf{e_n}, \tag{18}$$

with $\mathbf{e_n} = \frac{\mathbf{X}_i - \mathbf{X}_j}{\|\mathbf{X}_i - \mathbf{X}_j\|}$ as shown Fig. 2. The tangential overlap distance $\boldsymbol{\delta_t}$ is obtained by integrating the relative tangential velocity at the point of contact while the Coulomb's law is verified. Therefore, the tangential overlap distance $\boldsymbol{\delta_t}^{n+1}$ at the time step $n+1$ is obtained by

$$\boldsymbol{\delta_t}^{n+1} = \frac{1}{k_\mathrm{t}}(-\mu_c \|\mathbf{F}_n\|\mathbf{e_t} - \gamma_\mathrm{t}(\mathbf{U}_{i,j}\cdot\mathbf{e_t})\mathbf{e_t}), \tag{19}$$

when the particle is sliding (i.e., $\|\mathbf{F}_t\| > \mu_\mathrm{c}\|\mathbf{F}_n\|$), and by

$$\boldsymbol{\delta_t}^{n+1} = R_{\delta_t}\cdot\boldsymbol{\delta_t}^{n} + \int_{t^n}^{t^{n+1}} (\mathbf{U}_{i,j}\cdot\mathbf{e_t})\mathbf{e_t}\,dt, \tag{20}$$

when the particle is sticking to the obstacle (i.e., $\|\mathbf{F}_t\| \leqslant \mu_\mathrm{c}\|\mathbf{F}_n\|$). The rotation tensor R_{δ_t} moves $\boldsymbol{\delta_t}^n$ to the new local coordinate system at the state $n+1$, and

$$\mathbf{e_t} = \frac{-\boldsymbol{\delta_t} k_\mathrm{t} - \gamma_\mathrm{t}(\mathbf{U}_{i,j} - (\mathbf{U}_{i,j}\cdot\mathbf{e_n})\mathbf{e_n})}{\| -\boldsymbol{\delta_t} k_\mathrm{t} - \gamma_\mathrm{t}(\mathbf{U}_{i,j} - (\mathbf{U}_{i,j}\cdot\mathbf{e_n})\mathbf{e_n})\|}.$$

The parameters of the spring-dashpot model γ_n, γ_t, k_n, and k_t are calculated from the coefficient of normal (respectively, tangent) restitution $\xi_{\mathrm{max,n}}$ (respectively, $\xi_{\mathrm{max,t}}$) of dry collision

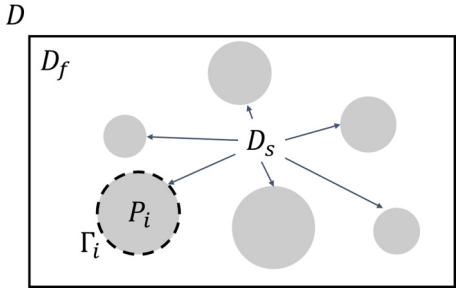

FIG. 3. Sketch of the decomposition for the domain D into a fluid domain D_f and the solid particles D_s.

and the contact time τ_c, as follows:

$$\begin{aligned} k_n &= \frac{m^*[\pi^2+\ln^2(\xi_{\max,n})]}{\tau_c^2}, \\ \gamma_n &= -\frac{2m^*\ln(\xi_{\max,n})}{\tau_c}, \\ k_t &= \frac{m_t^*[\pi^2+\ln^2(\xi_{\max,t})]}{\tau_c^2}, \\ \gamma_t &= -\frac{2m_t^*\ln(\xi_{\max,t})}{\tau_c}, \end{aligned} \tag{21}$$

with the effective mass

$$m^* = \frac{m_i m_j}{m_i + m_j}$$

and

$$m_t^* = m^* \frac{K^2}{K^2+1},$$

with $K^2 = 2/5$ the normalized radius of gyration for spherical particles.

The characteristics of the elastic properties of the particles are $\xi_{\max,n}$, $\xi_{\max,t}$, and τ_c. As noticed by Izard *et al.* [24], the relation between τ_c and k_n is unusual, but several studies show that the normal stiffness can be underestimated without modification of the dynamics of a dry system. Such assumption allows to reduce the simulation time since the collision characteristic time will be larger than the particle characteristic deformation time.

To ensure the stability of the model and the conservation of the momentum, Costa *et al.* [32] advised that the time step of the overall numerical algorithm Δt has to be chosen as a multiple of the contact time τ_c (at least during the collision). This condition guarantees a zero overlap at the end of the collision and allows the fluid to adapt itself to sudden changes in velocity of the colliding particles.

The force $\mathbf{F}_{i,\text{wall}}$ and the torque $\mathbf{T}_{i,\text{wall}}$ are assumed to be equivalent to the asymptotic case $\beta \to +\infty$ and $m_{P_j} \to +\infty$.

IV. NUMERICAL MODEL

In this section, the numerical methods used to solve the fluid as well as the particle dynamics are detailed in the first two subsections and summarized in Fig. 7. The local lubrication correction model is described in the last subsection.

A. Discretization of the governing equations

The governing equations considered are the incompressible Navier-Stokes equations for a viscous fluid:

$$\begin{aligned} \frac{\partial u_i}{\partial t} + \frac{\partial (u_i u_j)}{\partial x_j} &= -\frac{1}{\rho}\frac{\partial p}{\partial x_i} + \frac{\mu}{\rho}\frac{\partial}{\partial x_j}\left(\frac{\partial u_i}{\partial x_j}\right) + \chi\lambda(u_{\tau,i}-u_i), \\ \frac{\partial u_i}{\partial x_i} &= 0, \end{aligned} \tag{22}$$

where $(i;j) = \{1,2,3\}^2$, u_i are the velocity components, p is the pressure. The fluid is Newtonian with density ρ and dynamic viscosity μ. The system of Eq. (22) is solved on a uniform Cartesian mesh of the three dimensional domain $D = D_f \cup D_s$, where N spherical particles P_i forming the solid domain $D_s = \bigcup_{i=1}^{N} P_i$ with $P_i \cap P_j = \emptyset$ for $i \neq j$ and $D_f = D \setminus D_s$ is the fluid domain (see Fig. 3). The interface between the solid and fluid phases is denoted $\Gamma_s = \bigcup_{i=1}^{N} \Gamma_i$. Each particle P_i is assumed to be homogeneous with a density $\rho_{p,i}$ and a diameter $d_i = 2a_i$.

A no-slip boundary condition is implicitly imposed at the interface Γ_s, by the penalty term $\chi\lambda(u_{\tau,i} - u_i)$. Indeed, as reminded by Angot *et al.* [19], solving the penalized Eqs. (22) is equivalent to solving the incompressible Navier-Stokes equations in the fluid domain and to enforce a no-slip boundary condition at the boundary Γ_s when $\lambda \to +\infty$. The computation of the penalty term is detailed later.

The Navier-Stokes Eqs. (22) are discretized using a cell-centered collocated arrangement of the primitive variables (p,u_i). Face-centered velocities v_i are also introduced in addition to the cell-centered velocities u_i, to eliminate odd-even decoupling which can lead to large pressure variations in space [33].

The equations are integrated in time using the classical projection scheme introduced by Chorin [34] and Temam [35]. The system Eqs. (22) is then solved in the following four steps:

(1) *Prediction:* In this first step, the momentum equation is solved to obtain an intermediate virtual velocity u_i^*, starting from a guess for the pressure field q. We choose an incremental scheme so $q = p^n$. The convective and viscous terms are discretized in time by a second-order Adams-Bashforth scheme and an implicit Crank-Nicolson scheme, respectively. Hence, the following momentum Eq. (23) is solved at the cell-nodes:

$$\frac{u_i^* - u_i^n}{\Delta t} + \frac{1}{2}\left(3C_i^n - C_i^{n-1}\right) = -\frac{1}{\rho}\frac{\partial q}{\partial x_i} + \frac{\mu}{2\rho}\left(D_i^* + D_i^n\right), \tag{23}$$

where $C_i = \frac{\partial v_j u_i}{\partial x_j}$ and $D_i = \frac{\partial}{\partial x_j}(\frac{\partial u_i}{\partial x_j})$ are the convective and diffusive terms, respectively. Spatial derivatives $\frac{\partial}{\partial x}$ are approximated by a second-order central finite difference scheme. The gradients computed at cell-centers and face-centers are denoted $(\frac{\partial}{\partial x_i})_{cc}$ and $(\frac{\partial}{\partial x_i})_{fc}$.

The virtual face-centered velocities v_i^* are calculated as follows [33]:

$$\begin{aligned} \hat{u}_i &= u_i^* + \frac{\Delta t}{\rho}\left(\frac{\partial q}{\partial x_i}\right)_{cc}, \\ \hat{v}_1 &= \gamma_w \hat{u}_{P,1} + (1-\gamma_w)\hat{u}_{W,1}, \\ \hat{v}_2 &= \gamma_s \hat{u}_{P,2} + (1-\gamma_s)\hat{u}_{S,2}, \\ \hat{v}_3 &= \gamma_b \hat{u}_{P,3} + (1-\gamma_b)\hat{u}_{B,3}, \\ \hat{v}_i^* &= \hat{v}_i - \frac{\Delta t}{\rho}\left(\frac{\partial q}{\partial x_i}\right)_{fc}, \end{aligned} \tag{24}$$

where $\hat{\mathbf{u}}_P$, $\hat{\mathbf{u}}_W$, $\hat{\mathbf{u}}_S$, and $\hat{\mathbf{u}}_B$ are the velocities computed at the nodes P, W, S, and B, respectively (see Fig. 4). The weights γ_w, γ_s, and γ_b are corresponding to linear interpolation for the west, south and back face velocity components, respectively. The same approach is considered for the opposite faces.

(2) *Projection:* At the end of projection step, velocities u_i^* are *a priori* not divergence free. The projection step aims

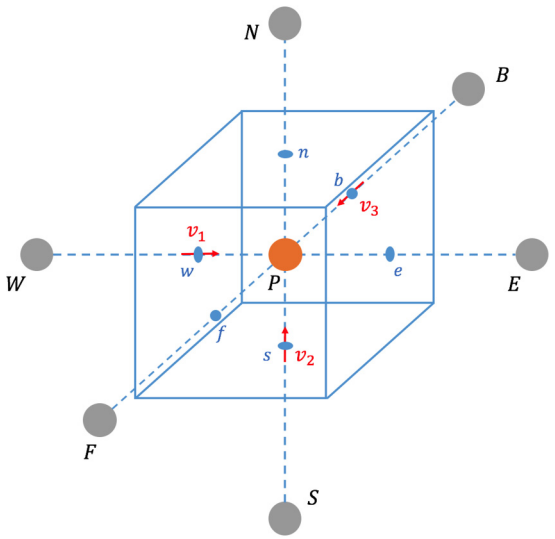

FIG. 4. Sketch of a grid cell with the notations used for the spatial discretization of the governing equations.

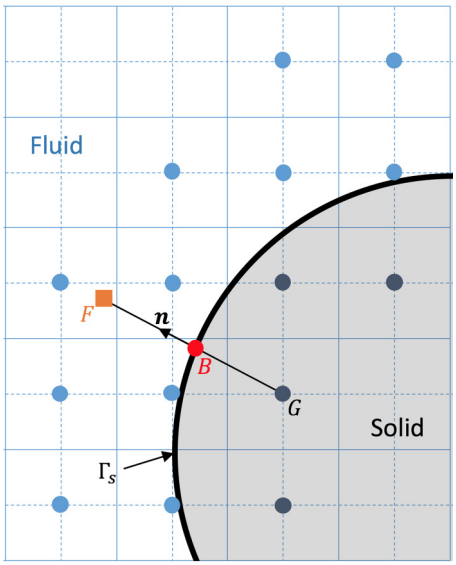

FIG. 5. Two-dimensional sketch of the IPC method. Velocity at the solid ghost point G is corrected using its symmetric F. The velocity at F is obtained by interpolation of the velocity of its four neighboring fluid points (eight neighbors in three-dimensional cases). The orthogonal projection of G at the particle surface is denoted B.

at finding the pressure field p^{n+1} such that $\nabla \cdot \widetilde{\mathbf{u}} = 0$. In particular, the equation

$$\frac{\widetilde{u}_i - u_i^*}{\Delta t} = \frac{1}{\rho}\frac{\partial p'}{\partial x_i} \tag{25}$$

is solved with the constraint that $\nabla \cdot \widetilde{\mathbf{u}} = 0$. Hence, the Poisson equation for the pressure correction p' is

$$\frac{1}{\rho}\frac{\partial}{\partial x_i}\left(\frac{\partial p'}{\partial x_i}\right) = \frac{1}{\Delta t}\frac{\partial v_i^*}{\partial x_i}, \tag{26}$$

with Neumann boundary conditions on the pressure on all boundaries (of D). Spatial derivatives $\frac{\partial}{\partial x}$ are approximated by a second-order central finite difference scheme.

The Poisson problem Eq. (26) is solved using the generalized minimal residual method (GMRES) developed by Saad *et al.* [36]. Preconditioners are used to reduce the number of iterations needed to ensure a divergence free velocity field, especially for low Reynolds flows.

(3) *Correction:* From the solution p' of the Poisson Eq. (26), the pressure and velocity fields $(p^{n+1}, \widetilde{\mathbf{u}})$ are updated as

$$\begin{aligned} p^{n+1} &= q + p', \\ \widetilde{u}_i &= u_i^* - \Delta t \frac{1}{\rho}\left(\frac{\partial p'}{\partial x_i}\right)_{\text{cc}}, \\ \widetilde{v}_i &= v_i^* - \Delta t \frac{1}{\rho}\left(\frac{\partial p'}{\partial x_i}\right)_{\text{fc}}, \end{aligned} \tag{27}$$

so that $\widetilde{\mathbf{u}}$ is divergence free. Gradients are discretized by second-order central finite difference scheme. Cell-centered and face-centered velocities are updated separately to improve the accuracy and stability of the prediction step.
The initial pressure is set arbitrarily to $p^0 = 0$.

(4) *Penalization:* This last step is performed after the resolution of the particle dynamics described in Sec. IV B (see Fig. 7). The velocity field $\widetilde{\mathbf{u}}$ is penalized using the particle velocities $\mathbf{U}^{n+1}$ to compute $\mathbf{u}^{n+1}$:

$$u_i^{n+1} = \frac{\widetilde{u}_i + \chi\lambda\Delta t u_{\tau,i}}{1 + \chi\lambda\Delta t}, \tag{28}$$

where λ is the penalty factor (arbitrary chosen in this article such that $\lambda = 10^8$). The characteristic function χ is defined for each cell center location $\mathbf{x}$ such that $\chi(\mathbf{x}) = 1$, if $\mathbf{x} \in D_s$ and the given cell has at least one neighbor in D_f. Everywhere else, $\chi(\mathbf{x}) = 0$.

The penalization is made using the second-order ghost-cell approach known as image point correction method (IPC) [37]. The main idea of the method is to find the right correction $u_{\tau,i}$ for all solid cells at the fluid-solid interface ($\chi = 1$) to impose the desired velocity at the interface Γ_s.

The IPC method, illustrated in Fig. 5, corrects the velocity at the solid ghost point G by

$$\mathbf{u}_\tau = \mathbf{u}_B + \phi\left(\frac{\partial \mathbf{u}}{\partial \mathbf{n}}\right)\Big|_{\phi=0}, \tag{29}$$

with $\mathbf{u}_B$ the solid velocity at the surface point B, $\mathbf{n}$ is the outward normal unit vector of the interface. The level set function ϕ is the signed distance from the boundary of the bodies with negative sign within the particles and positive one elsewhere. In particular, $\phi = 0$ at the interface Γ_s, and $|\phi|$ is the minimal distance to Γ_s.

The velocity $\mathbf{u}_B$ can be easily calculated from the velocity $\mathbf{U}$ and rotational velocity Ω of the particle mass center. The gradient $(\partial \mathbf{u}/\partial \mathbf{n})|_{\phi=0}$ is determined from $\mathbf{u}_B$ and the velocity $\mathbf{u}_F$ at F the symmetric point of G. The distance between B and F, as well as the outward normal vector $\mathbf{n}$ can be easily computed with the level set function ϕ.

The velocity at the point F is computed by interpolating the velocities of the eight closest fluid neighbors of F. If one of the eight neighbors is G, the surface point B is considered instead

of G. Interpolations are made using a second-order Lagrange interpolation scheme.

To ensure the stability of the whole numerical method, the time step Δt is adapted such that the Courant-Friedrichs-Lewy condition is satisfied: $\Delta t = \beta_\tau \Delta x / V_{\max}$, where $\beta_\tau \leqslant 1$ is chosen arbitrarily, Δx the characteristic length of the grid cells, and $V_{\max}$ is the maximum of the velocity absolute value computed on the grid cells. However, the time step does not change significantly between to two consecutive iterations. Therefore, the expression of the prediction step Eq. (23) is still valid.

When particles are in near contact, the time step Δt has to satisfy the stability condition of the collision model. Therefore, when lubrication corrections are active (i.e., collision might occur) Δt is chosen such that $\tau_c = N_t \Delta t$ (with τ_c the contact time) and $\Delta t \leqslant \beta_\tau \frac{\Delta x}{V_{\max}}$, with $N_t > 0$ an integer ($N_t \geqslant 8$, in this paper).

B. Dynamics of the particles

The particle dynamics is solved by a discrete element method (DEM) which is primarily devoted to multi-contact interactions for a large suspension [24]. The dynamics of each rigid particle is obtained by the following equations of conservation:

$$m_i \frac{d\mathbf{U}_i}{dt} = \mathbf{F}_i^{\text{hyd}} + \mathbf{F}_i^{\text{coll}} + \mathbf{F}_i^{\text{ext}}, \tag{30}$$

$$\frac{d J_i \Omega_i}{dt} = \mathbf{T}_i^{\text{hyd}} + \mathbf{T}_i^{\text{coll}}, \tag{31}$$

for a given particle P_i of mass m_i, inertia matrix J_i, linear velocity $\mathbf{U}_i$ of the mass center, and rotational velocity Ω_i. The hydrodynamic force and torque are denoted $\mathbf{F}_i^{\text{hyd}}$ and $\mathbf{T}_i^{\text{hyd}}$. Nonhydrodynamic forces like gravity (which is the only external force considered here) are denoted $\mathbf{F}_i^{\text{ext}}$. The force $\mathbf{F}_i^{\text{coll}}$ and torque $\mathbf{T}_i^{\text{coll}}$ represent the effects of solid contacts of P_i with obstacles (see Sec. III).

To numerically compute the hydrodynamic force and torque, the surface Γ_i of the particle P_i is meshed using $N_{\text{p},i}$ elements. The kth element of the mesh of Γ_i is denoted P_i^k and s_k is its surface. The set $\boldsymbol{L}(P_i^k)$ is defined as all the particles P_j, $j \neq i$ such that the distance between the surface of P_j and the center of P_i^k is lower than $a\epsilon_{\text{lub}}$. The distance $a\epsilon_{\text{lub}}$ is defined as the narrowest gap width between the center of the P_i^k and a potential nearby obstacle for the solver to fully resolve hydrodynamic interactions (see Fig. 6).

The total hydrodynamic force and torque on the particle P_i are given by

$$\begin{aligned} \mathbf{F}_i^{\text{hyd}} &= \mathbf{F}_i^{\text{solv}} + \mathbf{F}_i^{\text{deg}}, \\ \mathbf{T}_i^{\text{hyd}} &= \mathbf{T}_i^{\text{solv}} + \mathbf{T}_i^{\text{deg}}. \end{aligned} \tag{32}$$

The force $\mathbf{F}_i^{\text{deg}}$ and torque $\mathbf{T}_i^{\text{deg}}$ are defined as

$$\begin{aligned} \mathbf{F}_i^{\text{deg}} &= \int_{\substack{\mathbf{p}\in\Gamma_i, \\ \boldsymbol{L}(\mathbf{p})\neq\varnothing}} (\sigma\cdot\mathbf{n})\, dS, \\ \mathbf{T}_i^{\text{deg}} &= \int_{\substack{\mathbf{p}\in\Gamma_i, \\ \boldsymbol{L}(\mathbf{p})\neq\varnothing}} a_i\mathbf{n}\wedge(\sigma\cdot\mathbf{n})\, dS. \end{aligned} \tag{33}$$

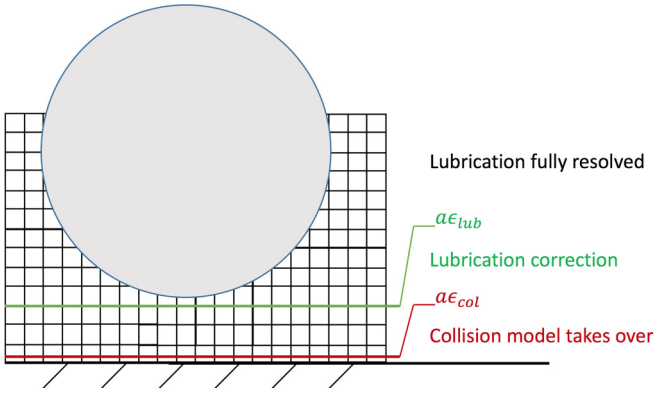

FIG. 6. Representation of the two parameters ϵ_{lub} and ϵ_{col} of the lubrication correction model. Typically, $a\epsilon_{\text{lub}} \sim$ 2–3 grid cells.

These two components of the hydrodynamics are underestimated by the numerical simulation due to the insufficient number of grid elements in the gap between the particle P_i and its surrounding obstacles, to properly capture the fluid flow. Therefore, a local lubrication correction model is introduced to balance the degraded hydrodynamics (see Sec. IV C). Lubrication correction on the force and torque are denoted $\mathbf{F}_i^{\text{lub}}$ and $\mathbf{T}_i^{\text{lub}}$.

The remaining of the hydrodynamics $\mathbf{F}_i^{\text{solv}}$ and $\mathbf{T}_i^{\text{solv}}$ are obtained via the flow solver, as follows:

$$\begin{aligned} \mathbf{F}_i^{\text{solv}} &= \int_{\substack{\mathbf{p}\in\Gamma_i, \\ \boldsymbol{L}(\mathbf{p})=\varnothing}} (\sigma\cdot\mathbf{n})\, dS, \\ \mathbf{T}_i^{\text{solv}} &= \int_{\substack{\mathbf{p}\in\Gamma_i, \\ \boldsymbol{L}(\mathbf{p})=\varnothing}} a_i\mathbf{n}\wedge(\sigma\cdot\mathbf{n})\, dS. \end{aligned} \tag{34}$$

The resolved hydrodynamics are computed by numerical integration of the fluid stress σ acting on all elements P_i^k far enough to nearby obstacles:

$$\begin{aligned} \mathbf{F}_i^{\text{solv}} &\approx \sum_{\substack{k\in[[1,N_{\text{p},i}]], \\ \boldsymbol{L}(P_i^k)=\varnothing}} (\sigma\cdot\mathbf{n})\, s_k, \\ \mathbf{T}_i^{\text{solv}} &\approx \sum_{\substack{k\in[[1,N_{\text{p},i}]], \\ \boldsymbol{L}(P_i^k)=\varnothing}} a_i\mathbf{n}\wedge(\sigma\cdot\mathbf{n})\, s_k. \end{aligned} \tag{35}$$

The fluid stress σ is interpolated of the pressure and velocities $(p, \mathbf{u}_i)$, using a second-order Lagrange scheme at the center of P_i^k.

Among the forces acting on the particle, the short-range hydrodynamics (lubrication) and collision forces have timescales smaller than the time scale associated with fluid flow. The particle dynamics is therefore computed at a smaller time step $\delta t = \frac{\Delta t}{n_t}$, with n_t arbitrary chosen large, to accurately integrate (in time) short-range interaction forces. Numerical simulations have shown that changing n_t between 10^2 and 10^3 does not affect significantly the results. Since the motion of the particles occurs at a time step smaller than Δt, it is not necessary to recompute the resolved hydrodynamic forces $\mathbf{F}_i^{\text{solv}}$ at each subtime step δt. Hence, particle dynamics is solved at each subtime step δt with updated short-range interactions and frozen resolved hydrodynamics. The discretized expressions of

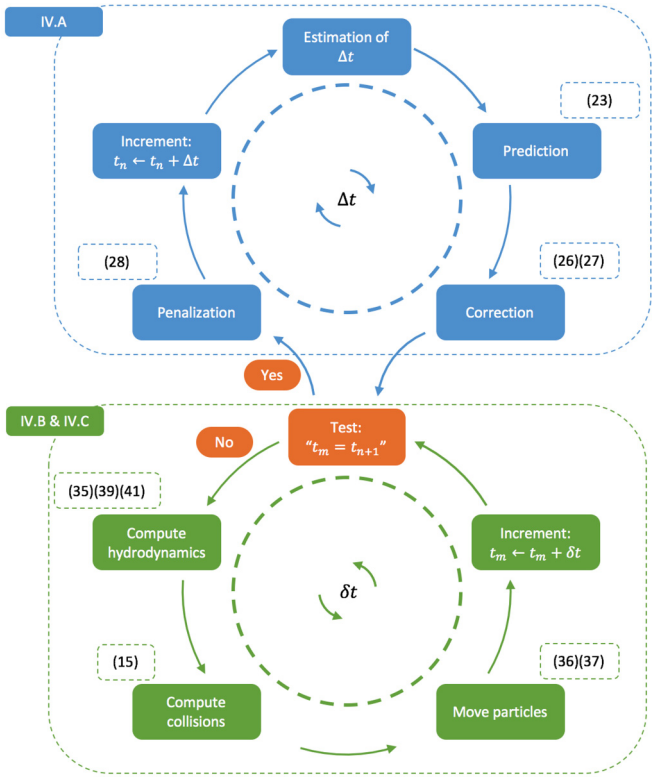

FIG. 7. Sketch description of the numerical algorithm used to compute the state $n+1$ of the whole system from its state n. The algorithm starts at the estimation of the time step Δt which is the time elapse between the system state n and $n+1$. The particle dynamics is solved in n_t sub-time steps $\delta t = \frac{\Delta t}{n_t}$. m denotes the current substate of the system between the state n and $n+1$ while the particle dynamics is computed. Dashed boxes contain the reference to the main equations computed at the given step.

Eqs. (30) and (31) are then written as

$$\mathbf{U}_i^{m+1} = \mathbf{U}_i^m + \frac{\delta t}{m_i}\left[\mathbf{F}_i^{\text{solv}}\right]^{n+1} + \frac{\delta t}{m_i}\left[\mathbf{F}_i^{\text{coll}} + \mathbf{F}_i^{\text{ext}} + \mathbf{F}_i^{\text{lub}}\right]^m, \tag{36}$$

$$\Omega_i^{m+1} = \left(J_i^{m+1}\right)^{-1}\left[J_i^m \Omega_i^m + \delta t\left(\left[\mathbf{T}_i^{\text{solv}}\right]^{n+1} + \left[\mathbf{T}_i^{\text{coll}} + \mathbf{T}_i^{\text{lub}}\right]^m\right)\right], \tag{37}$$

where m denotes the substate of the system at the time $t = t_n + m\delta t$ with t_n the time at the state n of the system. Since the particle dynamics is solved after the correction step but before the penalization (see Fig. 7), the force $[\mathbf{F}_i^{\text{solv}}]^{n+1}$ and torques $[\mathbf{T}_i^{\text{solv}}]^{n+1}$ are computed from the fields $(p^{n+1}, \tilde{\mathbf{u}})$ and not $(p^{n+1}, \mathbf{u}^{n+1})$.

C. The local lubrication correction model

The lubrication force $\mathbf{F}_i^{\text{lub}}$ and torque $\mathbf{T}_i^{\text{lub}}$ acting on P_i are given by

$$\begin{aligned} \mathbf{F}_i^{\text{lub}} &= \sum_{j \in [[1,N]] \setminus \{i\}} \mathbf{F}_{i,j}^{\text{lub}} + \mathbf{F}_{i,\text{wall}}^{\text{lub}}, \\ \mathbf{T}_i^{\text{lub}} &= \sum_{j \in [[1,N]] \setminus \{i\}} \mathbf{T}_{i,j}^{\text{lub}} + \mathbf{T}_{i,\text{wall}}^{\text{lub}}, \end{aligned} \tag{38}$$

where $\mathbf{F}_{i,j}^{\text{lub}}$ and $\mathbf{T}_{i,j}^{\text{lub}}$ are the lubrication force and torque acting on P_i, created by the interaction of P_i and P_j. The lubrication force and torque created by the interaction of the particle P_i with a wall are denoted $\mathbf{F}_{i,\text{wall}}^{\text{lub}}$ and $\mathbf{T}_{i,\text{wall}}^{\text{lub}}$, and are equivalent to the asymptotic case $\beta \to +\infty$.

From the lubrication theory detailed in section II, $\mathbf{F}_{i,j}^{\text{lub}}$ and $\mathbf{T}_{i,j}^{\text{lub}}$ are given by

$$\begin{aligned} \mathbf{F}_{i,j}^{\text{lub}} &= \left(\mathbf{F}_{i,j}^{\text{lub,sq}} + \mathbf{F}_{i,j}^{\text{lub,sh}}\right)\mathbb{1}_{[\epsilon_{\text{col}}, \epsilon_{\text{lub}}]}(\epsilon), \\ \mathbf{T}_{i,j}^{\text{lub}} &= \mathbf{T}_{i,j}^{\text{lub,sh}}\, \mathbb{1}_{[\epsilon_{\text{col}}, \epsilon_{\text{lub}}]}(\epsilon), \\ \frac{\mathbf{F}_{i,j}^{\text{lub,sq}}}{\pi \mu a U_{i,j}^{\text{sq}}} &= -\frac{6R_0^4}{4H_0^2}\frac{1}{\epsilon}\,\mathbf{e_n}, \\ \frac{\mathbf{F}_{i,j}^{\text{lub,sh}}}{\pi \mu a U_{i,j}^{\text{sh}}} &= \int_0^{R_0} [-P_0 R + \partial_Z V_0 - \partial_Z U_0] R dR\, \mathbf{e_t}, \\ \frac{\mathbf{T}_{i,j}^{\text{lub,sh}}}{\pi \mu a^2 U_{i,j}^{\text{sh}}} &= \int_0^{R_0} [\partial_Z U_0 - \partial_Z V_0] R dR\, \mathbf{e_n} \wedge \mathbf{e_t}, \\ U_{i,j}^{\text{sq}} &= U_i^{\text{sq}} - U_j^{\text{sq}}, \\ U_{i,j}^{\text{sh}} &= U_i^{\text{sh}} - U_j^{\text{sh}} + (\omega_i - \omega_j \beta) a, \end{aligned} \tag{39}$$

with

$$\begin{aligned} H_0 &= 1 + \frac{1}{2} a \alpha R_0^2, \\ \alpha &= \frac{\beta + 1}{a\beta}, \\ R_0 &= \frac{1}{\sqrt{\epsilon}}\sqrt{1 - (1 + \epsilon - \epsilon_{\text{lub}})^2}. \end{aligned} \tag{40}$$

The projected relative velocity of the two particles on the direction $\mathbf{e_n}$ and $\mathbf{e_t}$ are $U_{i,j}^{\text{sq}}$ and $U_{i,j}^{\text{sh}}$ (see Fig. 8).

The indicator function $\mathbb{1}_{[\epsilon_{\text{lub}}, \epsilon_{\text{col}}]}(\epsilon)$ is nonzero and equals to 1 only if $\epsilon_{\text{col}} \leqslant \epsilon \leqslant \epsilon_{\text{lub}}$. Hence, the lubrication model is switched off when the hydrodynamics is fully resolved ($\epsilon \geqslant \epsilon_{\text{lub}}$) and when the gap disappears ($\epsilon \leqslant \epsilon_{\text{col}}$).

The analytic expressions of $\mathbf{F}_{i,j}^{\text{lub,sh}}$ and $\mathbf{T}_{i,j}^{\text{lub,sh}}$ are not as simple as the expression of $\mathbf{F}_{i,j}^{\text{lub,sq}}$. Therefore, we choose to compute the shearing components by a numerical integration. Furthermore, numerical integration will be necessary if we want to add lower orders of the lubrication forces and torques. The force $\mathbf{F}_{i,j}^{\text{lub,sh}}$ and the torque $\mathbf{T}_{i,j}^{\text{lub,sh}}$ are integrated on n_{lub}

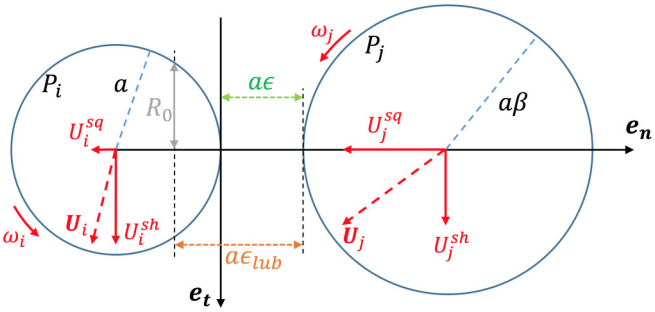

FIG. 8. Sketch of the two interacting particles with the notations used to evaluate $\mathbf{F}_{i,j}^{\text{lub}}$ and $\mathbf{T}_{i,j}^{\text{lub}}$.

subsets of the lubrication region $[0, R_0]$:

$$\frac{\mathbf{F}^{\mathrm{lub,sq}}_{i,j}}{\pi\mu a U^{\mathrm{sq}}_{i,j}} = \sum_{k=1}^{n_{\mathrm{lub}}} \int_{\boldsymbol{R}_k} [-P_0 R + \partial_Z V_0 - \partial_Z U_0] R dR \ \mathbf{e_t},$$
$$\frac{\mathbf{T}^{\mathrm{lub,sh}}_{i,j}}{\pi\mu a^2 U^{\mathrm{sh}}_{i,j}} = \sum_{k=1}^{n_{\mathrm{lub}}} \int_{\boldsymbol{R}_k} [\partial_Z U_0 - \partial_Z V_0] R dR \ \mathbf{e_n} \wedge \mathbf{e_t}, \tag{41}$$

where $\boldsymbol{R}_k = [\frac{k-1}{n_{\mathrm{lub}}} R_0, \frac{k}{n_{\mathrm{lub}}} R_0]$.

The local lubrication correction model (LLCM) is then built such that the total hydrodynamic force and torque acting on P_i are approximated by

$$\mathbf{F}^{\mathrm{hyd}}_i \approx \mathbf{F}^{\mathrm{solv}}_i + \mathbf{F}^{\mathrm{lub}}_i,$$
$$\mathbf{T}^{\mathrm{hyd}}_i \approx \mathbf{T}^{\mathrm{solv}}_i + \mathbf{T}^{\mathrm{lub}}_i. \tag{42}$$

Since the lubrication corrections $\mathbf{F}^{\mathrm{lub}}_{i,j}$ and $\mathbf{T}^{\mathrm{lub}}_{i,j}$ are the dominant orders of the hydrodynamics acting on the inner region of P_i, when the flow in the gap is in the Stokes regime (see Sec. II), $\mathbf{F}^{\mathrm{lub}}_i$ and $\mathbf{T}^{\mathrm{lub}}_i$ are not identical to the degraded hydrodynamics $\mathbf{F}^{\mathrm{deg}}_i$ and $\mathbf{T}^{\mathrm{deg}}_i$. Nevertheless, simulations presented in Sec. V show that the approximation $\mathbf{F}^{\mathrm{deg}}_i \approx \mathbf{F}^{\mathrm{lub}}_i$ can be made as long as the gap Reynolds numbers,

$$\mathrm{Re}^{\mathrm{gap}}_{i,j} = \frac{\rho a_i \epsilon \|\mathbf{U_i} - \mathbf{U_j}\|}{\mu},$$

remains small for all P_j in interaction with P_i during the simulations. In particular, the Reynolds number $\mathrm{Re}^{\mathrm{lub}}$ needs to be moderate (typically $\mathrm{Re}^{\mathrm{lub}} < 10^3$):

$$\mathrm{Re}^{\mathrm{lub}} = \frac{\rho \epsilon_{\mathrm{lub}} Q^{\max}}{\mu}, \tag{43}$$

with $Q^{\max} = \max_t [\max_{(i,j)\in[[1,N]]^2} (a_i \|\mathbf{U_i}(t) - \mathbf{U_j}(t)\|)]$.

This constraint also underlines the limitation of the LLCM to moderate Reynolds number flows. Indeed, inertia effects of the fluid in the gap are not corrected by the LLCM. Another limitation of the LLCM concerns the many-body interactions, which refers to the hydrodynamics action on a particle generated by nearby particles in interactions. Since the lubrication correction on P_i is only obtained by summing the corrections of the lubrication effects created by the interaction of P_i with other obstacles P_j [see Eq. (38)], the only many-body interactions considered are the ones resolved by the numerical method (included in $\mathbf{F}^{\mathrm{solv}}_i$).

V. RESULTS

The validation of the local lubrication correction model has been performed in two steps. First, the correction of the dominant component of the lubrication force (squeezing motion, Sec. II A) is validated by considering a single particle falling on a wall. Second, the oblique impact of a single particle on a wall is simulated to validate the corrections of the lubrication force and torque created by a sheared motion of the interstitial fluid.

A. Sphere falling on a wall

A single particle is immersed in a domain $[4d, 4d, 4d]$, with $d = 2a$ the particle diameter, uniformly meshed with cubic elements of size $\Delta x = \Delta y = \Delta z = hd$. Periodic boundary conditions are considered on the lateral faces of the domain. A no-slip boundary condition is imposed at the top and bottom walls (y constant). Simulations have been performed on a $[8d, 8d, 8d]$ domain (with $h = 1/40$) and have given identical solutions than on the smaller domain. The fluid is initially at rest and the particle is dropped without initial velocity such that the gap size from the bottom wall is given by $a\epsilon_{\mathrm{init}}$ as shown Fig. 9. The gravity field g acts on the y direction.

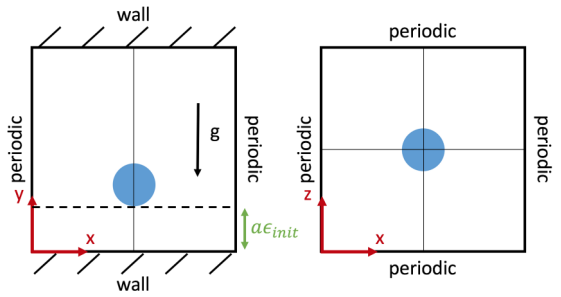

FIG. 9. Sketch of two cross-sections of the domain with its configuration and initial location of the particle.

To have an experimental reference for comparison, we chose the same configuration as one of the two cases from Harada *et al.* [38]. Particle and fluid properties are presented in Table I.

Under these configurations (Table I), the fluid characteristic Reynolds and Stokes numbers are as follows:

$$\mathrm{Re}_d = \frac{\rho U_T d}{\mu} \approx 25.7,$$
$$\mathrm{St}_d = \frac{\rho_p U_T d}{9\mu} \approx 3.27. \tag{44}$$

An *a posteriori* study shows that the maximum gap Reynolds number is

$$\mathrm{Re}^{\mathrm{gap}}_{i,\mathrm{wall}} = \frac{\rho a_i \epsilon \max(\|\mathbf{U_i}\|)}{\mu} \approx 0.92,$$

at $\epsilon \approx 0.31$. Therefore, the lubrication forces form the LLCM should reasonably approximate the degenerated forces: $\mathbf{F}^{\mathrm{deg}}_i \approx \mathbf{F}^{\mathrm{lub}}_i$.

1. Comparison with existing lubrication models

Figure 10 compares the particle velocity U simulated using the local lubrication correction model (LLCM) and a tabulated lubrication model (CLM, described below) to experimental

TABLE I. Simulation configurations.

Fluid density	ρ	985	$\mathrm{kg\,m^{-3}}$
Fluid dynamic viscosity	μ	0.142	Pa s
Particle density	ρ_{p}	1127	$\mathrm{kg\,m^{-3}}$
Particle diameter	d	0.0254	m
Normal restitution	$\xi_{\mathrm{max,n}}$	0.97	
Contact time	τ_{c}	$7.98 \cdot 10^{-5}$	s
Particle roughness	$a\epsilon_{\mathrm{col}}$	$2 \cdot 10^{-4} d$	m
Gravity field	g	9.781	$\mathrm{N\,kg^{-1}}$
Terminal velocity	U_{T}	0.146	$\mathrm{m\,s^{-1}}$
Initial position	ϵ_{init}	0.4181	

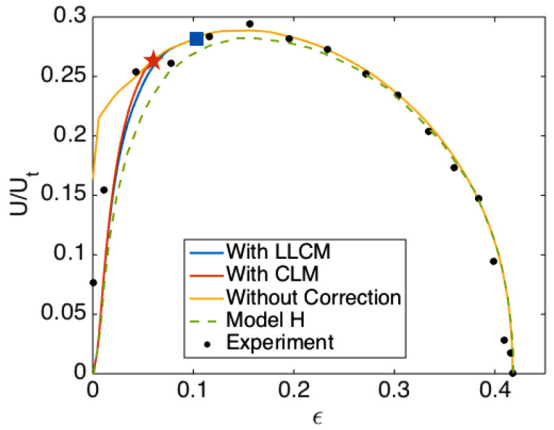

FIG. 10. Evolution of the vertical velocity of the particle versus the nondimensional gap size. Simulations using local (LLCM) and tabulated (CLM) lubrication correction are compared to Harada [38] experimental measurements and the model H. The LLCM and CLM are activated for ϵ smaller than the blue square and red star, respectively.

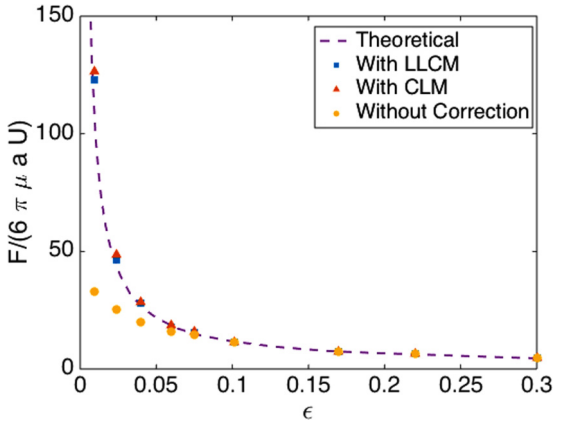

FIG. 11. Total hydrodynamic force as a function of ϵ in the case of a single particle approaching a solid wall. Simulations results are compared against the analytical solution of Brenner [39] (dashed line). All simulations are run with $h = 1/40$. The LLCM is activated on all ϵ smaller than $\epsilon_{\text{lub}} = 2\frac{\Delta y}{a}$.

measurements made by Harada *et al.* [38]. Numerical simulations were performed on a uniform Cartesian mesh with a grid spacing $h = 1/40$ and using $N_{\text{p}} = 3200$ elements for the particle surface mesh. Local lubrication corrections are performed on particle mesh elements closer than $2\Delta y$ to the wall. Numerical experiments have shown that the number of particle surface mesh elements (starting from about a thousand elements) has a limited impact on the solutions. Therefore, all the following simulations have been performed on particle surface meshes using $N_{\text{p}} = 3200$ elements.

The CLM [32] is a two-parameter model which corrects the normal component of the lubrication force on a spherical particle. The correction is made by adding $\Delta\mathbf{F}_i^{\text{lub}} = \Delta F_i^{\text{lub}}\,\mathbf{e_n}$ to the computed hydrodynamic force:

$$\frac{\Delta F_i^{\text{lub}}}{6\pi\mu a U_{i,\text{wall}}^{\text{sq}}} = \begin{cases} \lambda_{\text{w}}(\epsilon_{\Delta x}) - \lambda_{\text{w}}(\epsilon), & \epsilon_{\text{col}} \leqslant \epsilon < \epsilon_{\Delta x}, \\ \lambda_{\text{w}}(\epsilon_{\Delta x}) - \lambda_{\text{w}}(\epsilon_{\text{col}}), & 0 \leqslant \epsilon < \epsilon_{\text{col}}, \\ 0, & \text{otherwise}, \end{cases} \quad (45)$$

where $\mathbf{e_n}$ is defined as represented Fig. 8, and λ_{w} is the Stokes amplification factor for the lubrication interaction between a sphere and a wall:

$$\lambda_{\text{w}}(\epsilon) = \frac{1}{\epsilon} - \frac{1}{5}\ln(\epsilon) - \frac{1}{21}\epsilon\ln(\epsilon) + O(1). \quad (46)$$

Hence, the total hydrodynamic force is given by

$$\mathbf{F}_i^{\text{hyd}} = \int_{\Gamma_i} (\sigma \cdot \mathbf{n}) dS + \Delta\mathbf{F}_i^{\text{lub}}. \quad (47)$$

Aside from the computation of the hydrodynamics Eq. (47), the resolution of the fluid and particle dynamics is identical to the approach used for the LLCM.

The value of the parameter $\epsilon_{\Delta x}$ is determined by simulating the slow approach of a sphere to a wall, for a given grid cell resolution h. Figure 11 represents the total hydrodynamic force acting on a particle approaching a wall. A simulation without lubrication correction is compared to the analytical solution given by Brenner [39]. For $h = 1/40$ the value of $\epsilon_{\Delta x}$ is set to 0.06. Indeed, for $\epsilon \leqslant \epsilon_{\Delta x}$ the hydrodynamic force from the simulation without lubrication correction no longer matches the analytical solution [40] (see Fig. 11).

The relative errors L^2 and L^∞, between the particle velocity U obtained by a simulation and the experimental particle velocity U_{exp} provided by Harada *et al.* [38], are denoted $E_2(U) = \|U_{\text{exp}} - U\|_2$ and $E_\infty(U) = \|U_{\text{exp}} - U\|_\infty$, respectively. Both simulations are performed with CLM (Figs. 10 and 11) used $\epsilon_{\Delta x} = 0.06$ and $h = 1/40$. The CLM results are in good agreement with experimental measurement. As shown in Fig. 10, the Pearson's correlation coefficient is equal to 0.9661, $E_2(U_{\text{CLM}}) = 2.287 \times 10^{-3}\,\text{m s}^{-1}$, $E_\infty(U_{\text{CLM}}) = 1.229 \times 10^{-2}\,\text{m s}^{-1}$. The accuracy of the LLCM is comparable to the CLM. The simulated velocities remain close to experimental data (Pearson's correlation coefficient equals to 0.9633, $E_2(U_{\text{LLCM}}) = 2.385 \times 10^{-3}\,\text{m s}^{-1}$, and $E_\infty(U_{\text{LLCM}}) = 1.232 \times 10^{-2}\,\text{m s}^{-1}$). The computational time is about 10% more expansive with LLCM than CLM, without considering the computational cost of the tabulation. However, the computational time of the tabulation needed for the CLM can be significant. Furthermore, the LLCM can be extended to nonspherical particle while the CLM will require the tabulation of several parameters at a considerable CPU cost. The computational cost of the tabulation is also a CLM's limitation for polydisperse flows of spherical particles. Therefore, the LLCM is a reliable and efficient alternative to tabulated methods for complex flow particles.

Due to the lack of experimental measurements of the total hydrodynamic forces for a falling particle, total hydrodynamic forces obtained by numerical simulations are compared to an analytic model (model H) introduced by Harada *et al.* [38]. The model H is based on the Stokesian dynamic, where hydrodynamic forces $\mathbf{F}_i^{\text{Model\_H}} = \mathbf{F}_i^{\text{hyd}} + \mathbf{F}_i^{\text{lub}}$ on the particle are modeled by the dominant order of the lubrication force $\mathbf{f}_{\text{l}}$, the added-mass force $\mathbf{f}_{\text{a}}$, and the history Basset force $\mathbf{f}_{\text{Ba}}$.

The dominant order of the lubrication force is obtained by integration of the interstitial pressure between the particle and

the wall [41]:

$$\mathbf{f}_{\mathrm{l}} = 6\pi\mu a \frac{\mathbf{U}_i^{\mathrm{sq}}}{\epsilon}. \tag{48}$$

Since the motion of the particle is unsteady, the added mass force changes near the wall as follows [42,43]:

$$\begin{aligned} \mathbf{f}_{\mathrm{a}} &= m' \frac{d\mathbf{U}_i}{dt} + \frac{1}{2}\frac{dm'}{dt}\mathbf{U}_i, \\ m' &= \frac{2}{3}\pi\rho a^3 \left(1 + \sum_{i=0}^{\infty} \frac{3a^{(i+1)}}{f_0 f_1 \ldots f_i}\right), \end{aligned} \tag{49}$$

where f_i is recursively defined such that $f_0 = 2a(\epsilon + 1)$ and $f_i = f_0 - a^2/f_{i-1}$.The Basset history force for a spherical particle is given by

$$\mathbf{f}_{\mathrm{Ba}} = 6a^2\sqrt{\pi\rho\mu} \int_{-\infty}^{t} \frac{d\mathbf{U}_i}{dt'} \frac{dt'}{\sqrt{t - t'}}. \tag{50}$$

Hence, the total hydrodynamic force of the model H is $\mathbf{F}_i^{\mathrm{Model\_H}} = \mathbf{f}_{\mathrm{Ba}} + \mathbf{f}_{\mathrm{a}} + \mathbf{f}_{\mathrm{l}}$.

Numerical simulations have shown that velocities computed with the LLCM tend to experimental measurements as h decreases. Table II shows that the order of the numerical method used is close to a second order in L^2 and L^∞ on velocity when no lubrication corrections are applied. The particle dynamics for $h = 1/20$ is only fully resolved for large ϵ, where the lubrication forces are not dominant. Therefore, errors on the particle position and velocity are unexpectedly small for $h = 1/20$ compared to smaller h. Comparisons with Harada's measurements also show that the LLCM gives better results than model H for $h \leqslant 1/40$, even before any lubrication corrections (for the model H: Pearson's correlation coefficient equals to 0.9418, $E_2(U_{\mathrm{Model\_H}}) = 3.2 \times 10^{-3}\ \mathrm{m\,s^{-1}}$, $E_\infty(U_{\mathrm{Model\_H}}) = 1.3 \times 10^{-2}\ \mathrm{m\,s^{-1}}$).

TABLE II. Table of convergence for the particle position and velocity, when the particle dynamics is fully resolved ($\epsilon \geqslant 0.2$). The particle position Y_h and velocity U_h obtained with a grid mesh resolution h are compared to the particle position $Y_{1/100}$ and velocity $U_{1/100}$ obtained with a grid mesh resolution $h = 1/100$. The units of the position and velocity errors are m and $\mathrm{m\,s^{-1}}$.

	Velocity			
h	$\|U_{1/100} - U_h\|_2$	$\|U_{1/100} - U_h\|_\infty$	Order L^2	Order L^∞
1/20	2.13×10^{-4}	4.74×10^{-4}		
1/40	3.83×10^{-4}	6.35×10^{-4}	–	–
1/60	3.27×10^{-4}	5.48×10^{-4}	2.04	1.95
1/80	2.50×10^{-4}	3.75×10^{-4}	1.73	1.58
	Position			
h	$\|Y_{1/100} - Y_h\|_2$	$\|Y_{1/100} - Y_h\|_\infty$	Order L^2	Order L^∞
1/20	2.07×10^{-3}	2.08×10^{-3}		
1/40	7.95×10^{-4}	8.24×10^{-4}	1.81	1.81
1/60	3.64×10^{-4}	3.90×10^{-4}	1.62	1.62
1/80	1.44×10^{-4}	1.64×10^{-4}	1.54	1.53

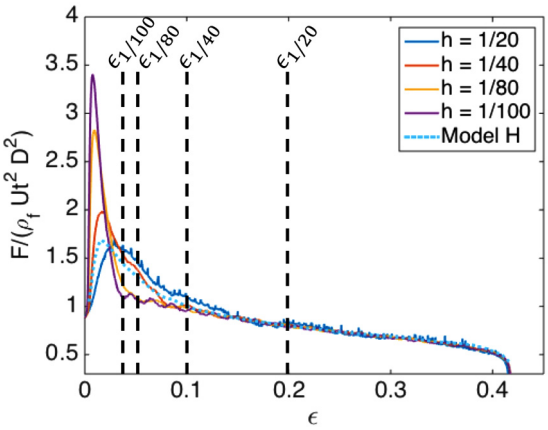

FIG. 12. Total hydrodynamic force, according to the y direction as a function of $1/\epsilon$ during the approach phase. For each grid mesh resolution h, lubrication correction is activated for $\epsilon \leqslant \epsilon_h$.

2. Grid sensitivity analysis

Using the same configuration described in Table I, simulations have been performed with four different background grid resolutions $h = 1/20$, $h = 1/40$, $h = 1/80$, and $h = 1/100$. The total hydrodynamic forces obtained are compared to the model H (Fig. 12).

Far from the wall ($\epsilon > 0.1$), higher grid resolutions ($h \leqslant 1/80$) improve the capture of the total hydrodynamic forces. Indeed, as shown on the Fig. 12, the hydrodynamic forces tend to the hydrodynamic forces of the model H which fits experimental velocities (Fig. 10). As the particle goes closer to the wall ($\epsilon < 0.1$), simulated hydrodynamic forces are lower than the solution of the model H, even before any lubrication correction is applied (see $h = 1/80$ and $h = 1/100$). Starting from the same initial conditions, the lower hydrodynamic forces induce higher particle velocities (than model H velocities) close to the wall. Therefore, the response of the LLCM is stronger close to the wall with steeper hydrodynamic forces than with the model H. However, the relevance of the model H as reference for $\epsilon < 0.1$ can be discussed since velocities of the model H do not perfectly fit experimental measurements in this range of ϵ (Fig. 10). As shown on Fig. 12, the LLCM has a lower hydrodynamic force compared to the model H. However, the particle velocity of the model H for $\epsilon < 0.1$ (Fig. 10) is lower than experimental data which implies that the model H overestimates the hydrodynamics when $\epsilon < 0.1$.

To assess the global rate of convergence of the LLCM, numerical simulations have been performed with different background grid resolutions h and with $\epsilon_{\mathrm{lub}} = 0.1$ fixed. The total hydrodynamic forces obtained are compared to the model H (Fig. 13).

Figure 14 shows that the global order of the numerical method used is first order in L^2 and L^∞ on position and velocity. However, one of the main features of the LLCM, which is to rely as much as possible on the solved fluid stress to compute the hydrodynamics, is ignored for the simulations using finer grid mesh resolution than $h = 1/40$. Therefore, the global order of convergence on velocity and position of the LLCM could be closer to a second order, since the computation of the hydrodynamics rely more and more (as h decrease)

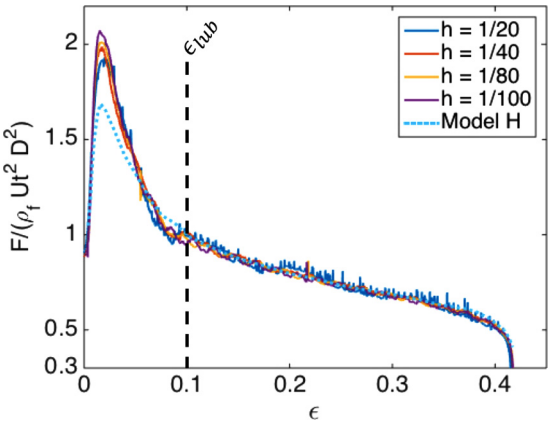

FIG. 13. Total hydrodynamic force, according to the y direction as a function of $1/\epsilon$ during the approach phase. For all curves, the lubrication correction is activated for $\epsilon \leqslant \epsilon_{\text{lub}}$.

on a numerical method without lubrication correction, which is a second order of convergence on position and velocity (see Table II). In addition, the LLCM is more accurate if ϵ_{lub} is adapted to the grid resolution h than if ϵ_{lub} is fixed. For instance with $h = 1/100$, the relative errors $E_2(U_{\text{LLCM}})$ and $E_\infty(U_{\text{LLCM}})$ are increased by 18.7% and 11.8% by using $\epsilon_{\text{lub}} = 0.1$ instead of $\epsilon_{\text{lub}} = \frac{2\Delta y}{a} (= 0.04)$.

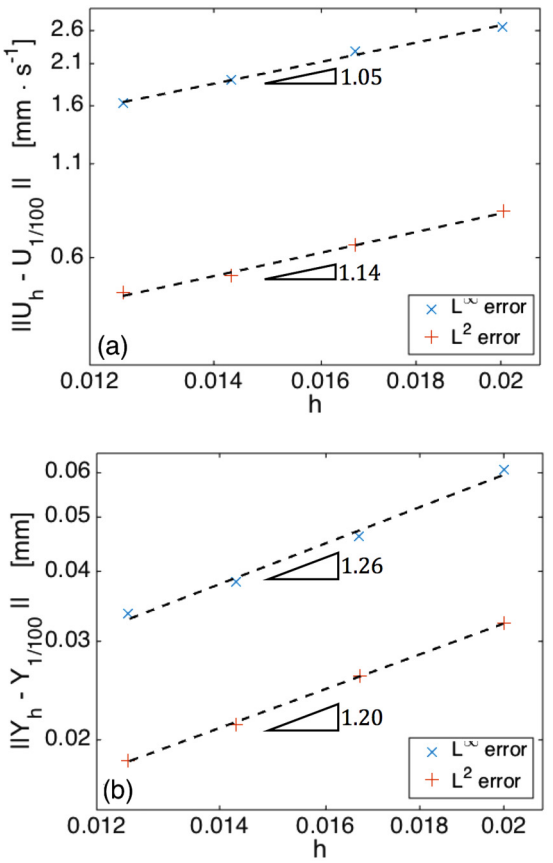

FIG. 14. Representation of the global rate of convergence on velocity (a) and position (b) of the particle center of gravity according to the norms L^2 and L^∞. The particle position Y_h and velocity U_h obtained with a grid mesh resolution h are compared to the particle position $Y_{1/100}$ obtained with a grid mesh resolution $h = 1/100$.

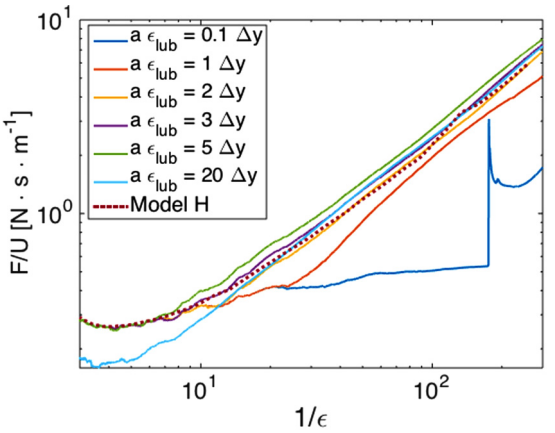

FIG. 15. Total hydrodynamic force, according to the y direction as a function of $1/\epsilon$ during the approach phase for the critical lubrication distances $a\epsilon_{\text{lub}}$ equal to $0.1\Delta y$, $1\Delta y$, $2\Delta y$, $20\Delta y$, $3\Delta y$, and $5\Delta y$ (by increasing F/U at the highest $1/\epsilon$). Grid mesh resolution is $h = 1/40$ for all curves.

3. *Sensitivity analysis from the lubrication parameter ϵ_{lub}*

The LLCM is a model with a single parameter ϵ_{lub} which sets the minimum gap length where lubrication corrections are needed. Several simulations have been made for different ϵ_{lub}. Figure 15 represents the total hydrodynamic force normalized by the particle velocity with respect to $1/\epsilon$.

Numerical simulations using $a\epsilon_{\text{lub}} \approx 2\Delta y$ are expected to give more realistic solutions since hydrodynamic forces better fit the solution of model H. For smaller ϵ_{lub}, hydrodynamic forces are underestimated leading to unrealistic mechanical contact and rebound of the particle (particle rebounds are not allowed by viscous effects for St < 10). Simulations with high ϵ_{lub} underestimate the total hydrodynamic force far from the wall, which decreases the solution accuracy.

The value of ϵ_{lub} depends on the spatial discretization of the Navier-Stokes equations and needs to be adapted to the numerical method. This configuration can be easily done by running a sensitivity analysis from ϵ_{lub}, as shown in this section.

4. *Analysis of the LLCM reliability during collision*

To complete our model reliability assessment, several simulations had been performed at higher Stokes numbers and compared to experimental data from Joseph *et al.* [44].

The conservation of the energy by the LLCM and the collision model have been checked by simulating the normal collision of a steel particle with a wall (see Fig. 16). When the particle is assumed elastic ($\xi_{\text{max,n}} = 1$) the energy is conserved during the collision. Otherwise, plastic deformations of the particle are mimicked by the collision model creating the observed energy dissipation. Figure 17 represents the distribution of the normalized effective coefficient of normal restitution of a particle versus the impact Stokes number. To be comparable to the measurements, we use the same technique and definition of the coefficient of normal restitution ξ_{n}, detailed by Joseph

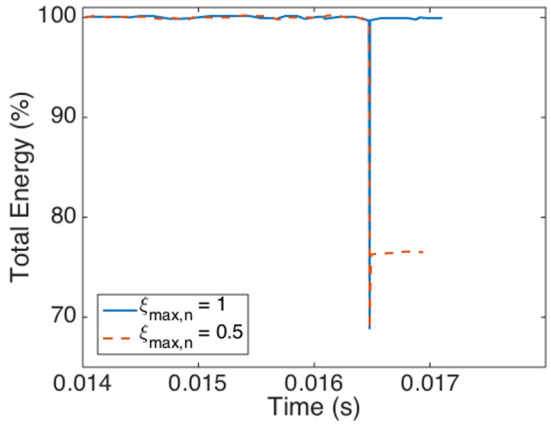

FIG. 16. Evolution of the total energy (energy potential and kinetic) of the system during an elastic ($\xi_{max,n} = 1$) or plastic ($\xi_{max,n} = 0.5$) collision of a steel particle with a wall. In both cases the impact Stokes number is $St_d \approx 6900$.

et al. [44]. By definition $\xi_n = -U_R/U_T$ where U_R is the particle rebound velocity and U_T is the terminal velocity of the particle before the collision.

When the fluid does not influence the dynamics of the particle while colliding with an obstacle (nonviscous fluids for instance), the effective coefficient ξ_n is maximum and is called dry coefficient of normal restitution $\xi_{max,n}$. Experimental measurements reported in Fig. 17 show that dry collision occurs at Stokes numbers, $St_d > 1000$, where lubrication forces become negligible compared to the particle inertia. At low Stokes numbers, $St_d \lesssim 200$, lubrication forces are dominant. For $St_d \sim 10$, lubrication effects prevent solid collision with the wall and maintain the particle in suspension above the wall.

Results with the local lubrication model (Fig. 17) are comparable to measurements and have a strong correlation with the experiment at a low Stokes number.

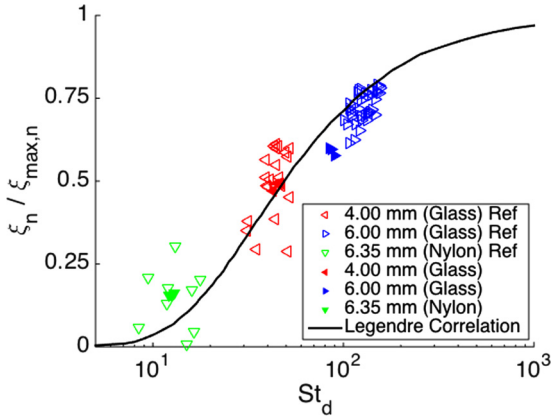

FIG. 17. Distribution of normalized effective coefficient of normal restitution $\xi_n/\xi_{max,n}$ of a single particle impacting a wall in respect of the particle Stokes number at the impact. Filled markers represent results obtained using the LLCM using the same experimental setup than Joseph *et al.* [44] (data represented by hallow markers). The black curve represents a correlation made on experimental data proposed by Legendre *et al.* [45]

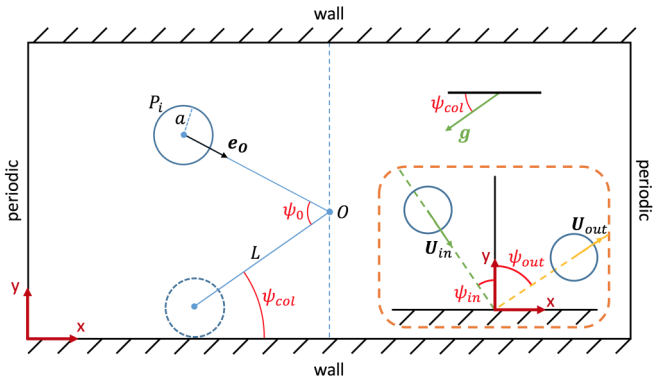

FIG. 18. Sketch of the simulation domain and initial location of the particle. Inside the dashed box, particle characteristic velocities and angles are displayed before and after collision with the wall.

B. Oblique impact of a particle on a wall

To validate the tangential component of the lubrication force, the oblique impact of a particle on a wall is the last case to validate our model. The same experimental setup than Joseph and Hunt [46], for oblique particle-wall collisions in the air and aqueous solutions, has been used.

A single particle is immersed in a domain $[19d,5d,3d]$ using a similar set-up than described in Sec. V A. The fluid is initially at rest and the particle is dropped without initial velocity as shown Fig. 18. To reproduce the experiment of Joseph and Hunt [46] the particle is linked to O by a virtual string of length $L = 10$ cm. The tension of the string is a virtual force $\mathbf{F}_i^T$ collinear to

$$\mathbf{e_0} = \frac{\mathbf{X}_O - \mathbf{X}_i}{\|\mathbf{X}_O - \mathbf{X}_i\|}$$

is added to the particle dynamic Eq. (30). The signed value of $(\mathbf{F}_i^T \cdot \mathbf{e_0})$ is found such that

$$\mathbf{U}_i \cdot \mathbf{e_0} = 0, \forall \|\mathbf{X}_O - \mathbf{X}_i\| \geqslant L + a. \tag{51}$$

The pendulum is released from an angle $\psi_0 = 18^\circ$ of its resting position ψ_{col} in contact with the wall (see Fig. 18). The gravity field $\mathbf{g}$ is oriented such that $\mathbf{g} = -g(\cos(\psi_{col})\mathbf{e_x} + \sin(\psi_{col})\mathbf{e_y})$ and $g = 9.81\ \mathrm{N\,kg^{-1}}$. Physical properties of the particle are presented in Table III and have been chosen according to Joseph and Hunt [46] experiments.

Numerical simulations using LLCM have shown that the parameter n_{lub}, introduced in the Sec. IV, has a limited impact on the results when $n_{lub} > 10$.

TABLE III. Particle properties.

		Glass	Steel	
Particle density	ρ_p	2540	7780	$\mathrm{kg\,m^{-3}}$
Particle diameter	d	0.0127	0.0127	m
Normal restitution	$\xi_{max,n}$	0.97	0.97	
Tangent restitution	$\xi_{max,t}$	0.39	0.34	
Contact time	τ_c	1×10^{-7}	1×10^{-7}	s
Friction coefficient	μ_c	0×10	0.11	
Friction coefficient (wet)	$\mu_{c,wet}$	0.15	0.02	
Particle roughness	$a\epsilon_{col}$	$2 \times 10^{-3}d$	$5 \times 10^{-4}d$	m

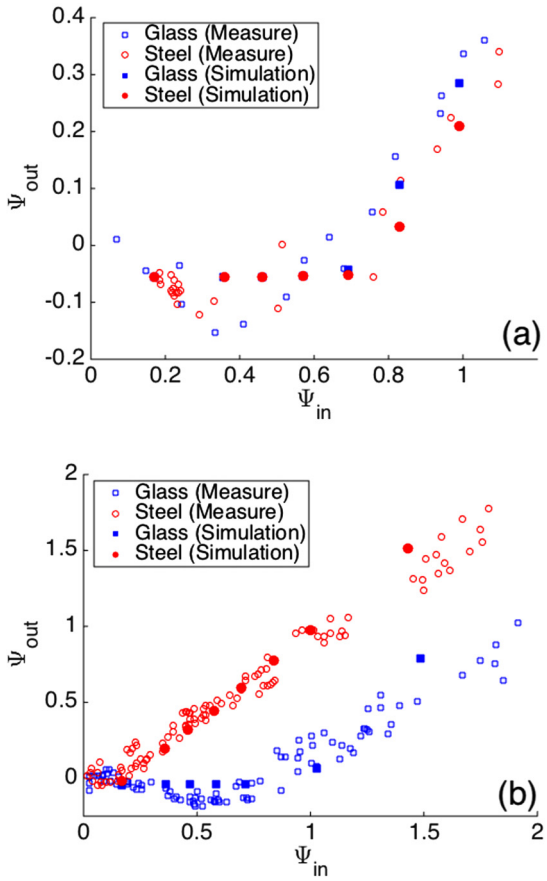

FIG. 19. Comparison between the normalized incidence Ψ_{in} and rebound Ψ_{out} angles of steel and glass particles in aqueous solution (a) or in the air (b). Results of simulations are represented by filled dots and are compared to Joseph and Hunt [46] experimental measurements (by circles).

Figure 19 shows a comparison between the normalized incidence $\Psi_{in} = \tan(\psi_{in})$ and rebound $\Psi_{out} = \tan(\psi_{out})$ angles obtained from oblique collisions between steel and glass spheres in the air or water. In practice, Ψ_{in} and Ψ_{out} have been assessed using the following equations:

$$\Psi_{in} = -\frac{\mathbf{V}_{C,in} \cdot \mathbf{e_x}}{\mathbf{V}_{C,in} \cdot \mathbf{e_y}}, \quad \Psi_{out} = \frac{\mathbf{V}_{C,out} \cdot \mathbf{e_x}}{\mathbf{V}_{C,out} \cdot \mathbf{e_y}}, \tag{52}$$

with $\mathbf{V}_{C,in}$ and $\mathbf{V}_{C,out}$ the velocities of the particle at the contact point, $\mathbf{V}_C = \mathbf{U}_i - a\,\Omega_i \wedge \mathbf{e_y}$, just before and just after collision, respectively.

As highlighted by Joseph and Hunt [46], piezoviscous effects in wet collision modify the coefficient of friction. Therefore, the modified (wet) friction coefficient (see Table III) is considered when the particle is immersed in water.

Numerical simulations have been performed with $h = 1/40$ using $N_p = 3200$ particle mesh elements. Lubrication parameters have been chosen as $\epsilon_{lub} = 2$ and $n_{lub} = 100$.

Collisions of the particle immersed in the air are called dry collisions since the interactions between the solid particle and the surrounding fluid are negligible. Simulations of dry collisions have been performed (Fig. 19, top) to validate the collision model and to assess the collision model accuracy with neglectable lubrication effects.

For wet collisions (Fig. 19 bottom), hydrodynamic effects are no longer negligible. Therefore, the accuracy of the lubrication correction can be assessed. The overall numerical simulations are in good agreement with the experimental data for the entire range of incidence angles.

VI. CONCLUSION AND OUTLOOK

A local lubrication correction model for particle-laden flow of spherical solid particles has been presented and validated. Interactions between a particle and an obstacle (another particle or a wall) can be decomposed into three types: long-range hydrodynamics, short-range hydrodynamics also called lubrication effects, and mechanical solid-solid contacts.

Long-range hydrodynamic interactions are fully resolved by our numerical solver based on the volume penalization method (VP). The incompressible Navier-Stokes equations have been discretized in time using a scalar projection method and in space with a full second-order penalty method.

Due to unresolved scales associated with the grid, short-range hydrodynamic interactions are only partially captured by the numerical approach. We thus introduce a local lubrication model. This correction is based on asymptotic expansions of analytical solutions of particle-particle or particle-wall interactions, assuming that the flow within the gap between the particle and the obstacle is in the Stokes regime. Lubrication forces and torques are corrected in a neighborhood of the contact point of two interacting particles where lubrication is poorly captured, as long as the normalized gap width ϵ is smaller than a critical length ϵ_{lub} (a model parameter).

Finally, a linear soft-sphere collision model is used for solid-solid contacts. This model, widely used in the literature [24,32], represents mechanical contacts as two spring-dashpot systems connected at the contact point. The model allows stretching the collision time, to avoid computational overhead in the calculation of the collision force, making the method computationally efficient.

Our local lubrication correction model has been validated on several benchmarks. First, we considered a single particle falling onto a wall at various approach velocities. The comparison with experimental results [38,44] enables us to validate the dominant lubrication component resulting from the squeezing of the fluid in the gap. The lubrication force and torque created by the shearing of the fluid in the gap have been validated on oblique particle-wall collisions in dry and wet systems proposed by Joseph and Hunt [46]. Since lubrication corrections are made locally, our lubrication model does not require tabulation and is compatible with nonspherical particles. The model will be tested for polydisperse flows of ellipsoidal particles in future works.

ACKNOWLEDGMENTS

The simulations presented in this paper were carried out using the PLAFRIM experimental parallel testbed, being developed under the Inria PlaFRIM development action with support from LaBRI and Institut de Mathématiques de Bordeaux and other entities: Conseil Régional d'Aquitaine, FeDER, Université de Bordeaux and CNRS [47].

[1] R. Sun and H. Xiao, CFD-DEM simulations of current-induced dune formation and morphological evolution, Adv. Water Resour. **92**, 228 (2016).

[2] J. Frohlich, B. Vowinckel, T. Kempe, and V. I. Nikora, *Numerical Simulation of Sediment Transport in Open Channel Flow* (Taylor & Francis, London, 2012).

[3] J. F. Morris, R. Mari, R. Seto, and M. M. Denn, Shear thickening, frictionless and frictional rheologies in non-Brownian suspensions, J. Rheol. **58**, 1693 (2014).

[4] A. Sierou and J. F. Brady, Accelerated Stokesian dynamics simulations, J. Fluid Mech. **448**, 115 (2001).

[5] E. Climent and M. R. Maxey, Numerical simulations of random suspensions at finite Reynolds numbers, Int. J. Multiphase Flow **29**, 579 (2003).

[6] M. R. Maxey and B. K. Patel, Localized force representations for particles sedimenting in Stokes flow, Int. J. Multiphase Flow **27**, 1603 (2001).

[7] D. D. Joseph H. H. Hu, and M. J. Crochet, Direct simulation of fluid particle motions, Theor. Comput. Fluid Dyn. **3**, 285 (1992).

[8] A. A. Johnson and T. E. Tezduyar, 3D simulation of fluid-particle interactions with the number of particles reaching 100, Comput. Methods Appl. Mech. Eng. **145**, 301 (1982).

[9] S.V. Apte, M. Martin, and N. A. Patankar, A numerical method for fully resolved simulation (FRS) of rigid particle-flow interactions in complex flows, J. Comput. Phys. **228**, 2712 (2009).

[10] T. W. Pan, R. Glowinski, and J. Periaux, Distributed Lagrange multiplier methods for incompressible viscous flow around moving rigid bodies, Comput. Methods Appl. Mech. Eng. **151**, 181 (1998).

[11] N. Sharma and N. A. Patankar, A fast computation technique for the direct numerical simulation of rigid particulate flows, J. Comput. Phys. **205**, 439 (2005).

[12] J. A. Simeonov and J. Calantoni, Modeling mechanical contact and lubrication in direct numerical simulations of colliding particles, Int. J. Multiphase Flow **46**, 38 (2014).

[13] A. Wachs, A DEM-DLM/FD method for direct numerical simulation of particulate flows: Sedimentation of polygonal isometric particles in a Newtonian fluid with collisions, Comput. Fluids **38**, 1608 (2009).

[14] X. Shao, Z. Yu, and A. Wachs, A fictitious domain method for particulate flows with heat transfer, J. Comput. Phys. **217**, 424 (2006).

[15] B. Merlet, A. Lefebvre-Lepot, and T. N. Nguyen, An accurate method to include lubrication forces in numerical simulations of dense Stokesian suspensions, J. Fluid Mech. **769**, 369 (2015).

[16] A. J. C. Ladd and R. Verberg, Lattice-Boltzmann simulations of particle-fluid suspensions, J. Stat. Phys. **104**, 1191 (2001).

[17] Z. G. Feng and E. E. Michaelides, Proteus: A direct forcing method in the simulations of particulate flow, J. Comput. Phys. **202**, 20 (2005).

[18] M. Uhlmann, An immersed boundary method with direct forcing for the simulation of particulate flows, J. Comput. Phys. **209**, 448 (2005).

[19] P. Angot, C.-H. Bruneau, and P. Fabrie, A penalization method to take into account obstacles in incompressible flows, Numer. Math. **81**, 497 (1999).

[20] F. Radjai and F. Dubois, *Discrete-element Modeling of Granular Materials* (Wiley, New York, 2011).

[21] L. Lobry, S. Gallier, E. Lemaire, and F. Peters, A fictitious domain approach for the simulation of dense suspensions, J. Comput. Phys. **256**, 367 (2014).

[22] M. D. A. Cooley and M. E. O'Neill, On the slow motion generated in a viscous fluid by the approach of a sphere to a plane wall or stationary sphere, Mathematika **16**, 37 (1969).

[23] M. E. O'Niell and K. Stewartson, On the slow motion of a sphere parallel to a nearby plane wall, J. Fluid Mech. **27**, 705 (1967).

[24] T. Bonometti, E. Izard, and L. Lacaze, Modelling the dynamics of a sphere approaching and bouncing on a wall in a viscous fluid, J. Fluid Mech. **747**, 422 (2014).

[25] J. Wells, Y. Nguyen, and H. Truong, A fictitious-domain simulation of solid-liquid flow with subgrid lubrication force correction: A sphere falling onto a plane surface, Proc. Hydraul. Eng. **51**, 151 (2007).

[26] R. G. Cox, The motion of suspended particles almost in contact, Int. J. Multiphase Flow **1**, 343 (1974).

[27] O. R. Walton, *Numerical Simulation of Inelastic, Frictional Particle-Particle Interactions* (Butterworth-Heinemann, London, 1993).

[28] S. Kim and S. Karrila, *Microhydrodynamics: Principles and Selected Applications* (Dover Publications, New York, 1991).

[29] D. J. Jeffrey, Low Reynolds number flow between converging spheres, Mathematika **29**, 58 (1982).

[30] M. Stimson and G. B. Jeffery, The motion of two spheres in a viscous fluid, Roy. Soc. **111**, 110 (1926).

[31] J. Happel and H. Brenner, *Low Reynolds Number Hydrodynamics*, edited by M. Nijhoff (Springer, Netherlands, 1983).

[32] J. Westerweel, P. Costa, B. J. Boersma, and W. P. Breugem, Collision model for fully resolved simulations of flows laden with finite-size particles, Phys. Rev. E **92**, 053012 (2015).

[33] M. Bozkurttas, F. M. Najjar, A. Vargas, R. Mittal, H. Dong, and A. von Loebbecke, A versatile sharp interface immersed boundary method for incompressible flows with complex boundaries, J. Comput. Phys. **227**, 4825 (2008).

[34] A. J. Chorin, Numerical solution of the Navier-Stokes equations, Math. Comput. **22**, 745 (1968).

[35] R. Temam, Sur l'approximation de la solution des équations de Navier-Stokes par la méthode des pas fractionnaires II, Arch. Ration. Mech. Anal. **32**, 377 (1969).

[36] Y. Saad and M. H. Schultz, GMRES: A generalized minimal residual algorithm for solving nonsymmetric linear systems, SIAM J. Sci. and Stat. Comput. **7**, 856 (1986).

[37] J. Hovnanian, M. Bergmann, and A. Iollo, An accurate cartesian method for incompressible flows with moving boundaries, Commun. Comput. Phys. **15**, 1266 (2014).

[38] T. Tanaka, S. Harada, and Y. Tsuji, Fluid force acting on a particle falling toward a wall, JSME Int. J., Ser. B **44**, 520 (2001).

[39] H. Brenner, The slow motion of a sphere through a viscous fluid towards a plane surface, Chem. Eng. Sci. **16**, 242 (1961).

[40] W. P. Breugem, A combined soft-sphere collision/immersed boundary method for resolved simulations of particulate flows, *ASME 2010 3rd Joint US-European Fluids Engineering Summer Meeting*, Vol. 1 (2010), p. 2381.

[41] M. J. Adams and V. Perchard, The cohesive forces between particles with interstitial liquid, Inst. Chem. Eng. Symp. **91**, 147 (1985).

[42] S. L. Soo, *Fluid Dynamics of Multiphase Systems* (Blaisdell Publishing Company, Waltham, MA, 1967).

[43] H. Lamb, *Hydrodynamics*, 6th ed. (Dover Publications, New York, 1945).

[44] M. L. Hunt G. G. Joseph, R. Zenit, and A. M. Rosenwinkel, Particle-wall collisions in a viscous fluid, J. Fluid Mech. **433**, 329 (2001).

[45] C. Daniel, D. Legendre, and P. Guiraud, Experimental study of a drop bouncing on a wall in a liquid, Phys. Fluids **17**, 097105 (2005).

[46] G. G. Joseph and M. L. Hunt, Oblique particle-wall collisions in a liquid, J. Fluid Mech. **510**, 71 (2004).

[47] https://www.plafrim.fr/en/home/.